ABSTRACT

Title of dissertation: STUDIES OF COMPLEX SYSTEMS
IN CONDENSED MATTER PHYSICS
AND ECONOMICS

Anand Banerjee, Doctor of Philosophy, 2008

Dissertation directed by: Professor Victor M. Yakovenko
Department of Physics

This dissertation reports the study of complex systems from two very different fields. The dissertation is divided into two parts. The first part involves study of angular magnetoresistance in quasi-one-dimensional organic conductors and graphene bilayers (chapter 2 and 3). The second part is devoted to the modeling and empirical study of personal income distribution (chapter 4 and 5).

First, we study the effect of crystal superstructures, produced by orientational ordering of the ReO_4 and ClO_4 anions in the quasi-one-dimensional organic conductors $(TMTSF)_2ReO_4$ and $(TMTSF)_2ClO_4$, on the angular magnetoresistance oscillations (AMRO) observed in these materials. Folding of the Brillouin zone due to anion ordering generates effective tunneling amplitudes between distant chains. These amplitudes cause multiple peaks in interlayer conductivity for the magnetic field orientations along the rational crystallographic directions (the Lebed magic angles). Different wave vectors of the anion ordering in $(TMTSF)_2ReO_4$ and $(TMTSF)_2ClO_4$ result in the odd and even Lebed angles, as observed experimentally. When a strong magnetic field is applied parallel to the layers and perpendicular the chains and exceeds a certain threshold, the interlayer tunneling between different branches of the folded electron spectrum becomes possible, and interlayer conductivity should increase sharply. This effect can be utilized to probe the anion ordering gaps in $(\mathrm{TMTSF})_2\mathrm{ClO}_4$ and $(\mathrm{TMTSF})_2\mathrm{ReO}_4$. An application of this effect to κ-$(\mathrm{ET})_2\mathrm{Cu(NCS)}_2$ is also briefly discussed. Next, we study AMRO in graphene bilayers. We calculate the interlayer conductivity and investigate the effects of a parallel magnetic field on the low energy bands of graphene bilayer.

Next, we analyze the data on personal income distribution from the Australian Bureau of Statistics. We compare fits of the data to the exponential, log-normal, and gamma distributions. The exponential function gives a good (albeit not perfect) description of 98% of the population in the lower part of the distribution. The log-normal and gamma functions do not improve the fit significantly, despite having more parameters, and mimic the exponential function. We find that the probability density at zero income is not zero, which contradicts the log-normal and gamma distributions, but is consistent with the exponential one. The high-resolution histogram of the probability density shows a very sharp and narrow peak at low incomes, which we interpret as the result of a government policy on income redistribution. We also analyze data on individual income from Internal Revenue Service and University of Maryland. Finally, we discuss a model which captures the two-class structure of income distribution in the USA.

STUDIES OF COMPLEX SYSTEMS IN CONDENSED MATTER PHYSICS AND ECONOMICS

by

Anand Banerjee

Dissertation submitted to the Faculty of the Graduate School of the
University of Maryland, College Park in partial fulfillment
of the requirements for the degree of
Doctor of Philosophy
2008

Advisory Committee:

Professor H. Dennis Drew
Professor Theodore L. Einstein
Professor Christopher Jarzynski
Professor John D. Weeks
Professor Victor M. Yakovenko, Chair/Advisor

This dissertation is dedicated to my family.

ACKNOWLEDGMENTS

This research project would not have been possible without the support of many people. I wish to express my gratitude to my advisor, Professor Victor M. Yakovenko who was always been very helpful, patient and offered invaluable assistance, support and guidance. Working with him has been a wonderful experience.

I thank Professors Theodore. L. Einstein, H. Dennis Drew, Christopher Jarzynski and John. D. Weeks for agreeing to serve in my dissertation committee. There comments and suggestions were particularly helpful in improving my thesis.

I thank Professor Steve Anlage and Professor Rajarshi Roy. Professor Anlage gave me the opportunity to participate in the experimental research in his lab in my first year of graduate study and Professor Roy allowed me to attend his group meetings during the days when I did not have an academic advisor.

I would also like to thanks CNAM, Center for Superconductivity and MERSEC for providing financial assistance during various stages of my graduate study.

Special thanks also to all my graduate friends, especially my friends in the squash club. Winning the NCSRA division 4 championship with them was an experience that I would never forget.

TABLE OF CONTENTS

LIST OF TABLES

LIST OF FIGURES

Chapter 1

Introduction

1.1 Angular magnetoresistance oscillations

The quasi-one-dimensional (Q1D) organic conductors (TMTSF)$_2$X (where TMTSF is tetramethyltetraselenafulvalene, and X represents a monovalent anion, such as PF$_6$, ClO$_4$, or ReO$_4$) have very interesting physical properties, including the quantum Hall effect and possibly triplet superconductivity [1, 2]. Fig. 1.1 shows the schematic diagram of Q1D conductors. These materials consist of parallel conducting chains along the x axis, arranged in layers with the interchain spacing b along the y axis and the interlayer spacing c along the z axis. The electron tunneling amplitudes between the TMTSF molecular sites $t_a \gg t_b \gg t_c$ are estimated as 250 meV, 25 meV, 1.5 meV [1].

These materials exhibit the angular magnetoresistance oscillations (AMRO), where resistivity strongly changes as a function of the magnetic field orientation. Fig. 1.2, 1.3 and 1.4 show the three basic types of AMRO: the Lebed magic angles [3, 4, 5, 6, 7, 8] for the magnetic field rotation in the (y, z) plane, the Danner-Kang-Chaikin (DKC) oscillations in the (x, z) plane [9, 10], and the third angular effect in the (x, y) plane [11, 12, 13]. The Lebed oscillations manifest themselves as sharp peaks in the interlayer conductivity σ_{zz} occurring when the magnetic field points from one chain to another along a rational crystallographic direction, as

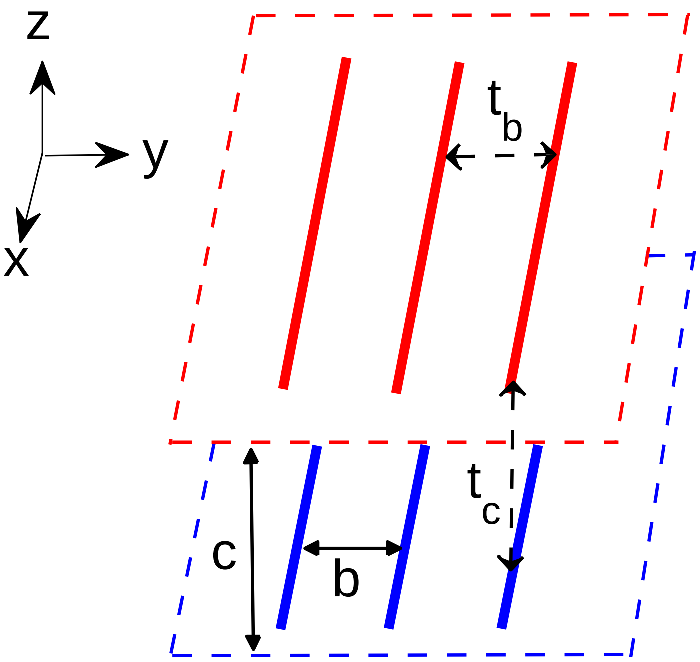

Figure 1.1: The figure shows the schematic diagram of quasi-one-dimensional organic conductors. TMTSF molecules form long conducting chains (shown by red and blue lines), arranged into layers with interchain spacing b and interlayer spacing c.

illustrated in Fig. 1.5. Approximating the triclinic crystal lattice of $(\mathrm{TMTSF})_2\mathrm{X}$ by the orthogonal one, the magic Lebed angles can be written as

$$\frac{B_y}{B_z}\frac{c}{b} = \frac{n}{m} \quad \Leftrightarrow \quad \sin\varphi\,\tan\theta = \frac{n}{m}\frac{b}{c}, \tag{1.1}$$

where n and m are integer numbers, and $\boldsymbol{B} = (B_x, B_y, B_z) = B(\sin\theta\cos\varphi, \sin\theta\sin\varphi, \cos\theta)$ is the magnetic field. Experimentally, the Lebed effect is the most pronounced for $m = 1$. Lee and Naughton [14, 15] studied AMRO for generic orientations of $\boldsymbol{B}$, where all three effects coexist. They found that the Lebed oscillations are enhanced when $B_x \neq 0$ [14], and the DKC oscillations still exist in the presence of $B_y \neq 0$ [15].

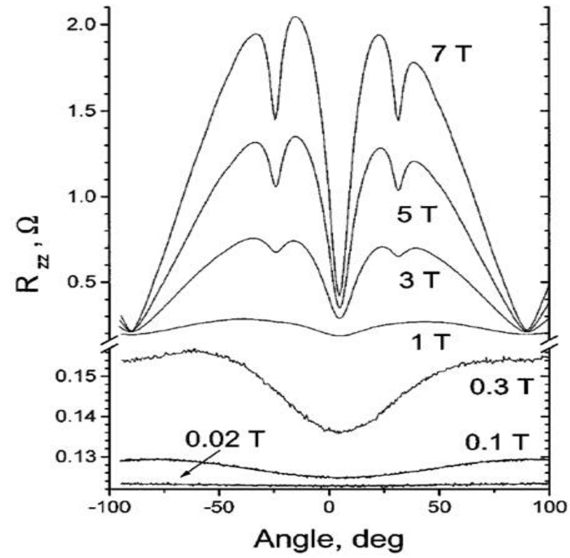

Figure 1.2: Figure shows the oscillations in the interlayer resistance R_{zz} as a function of the orientation of the magnetic field (rotated in the (x, y) plane). Lebed Magic Angles are the angles at which sharp dips are observed in R_{zz}. The plot was obtained from Ref. [6].

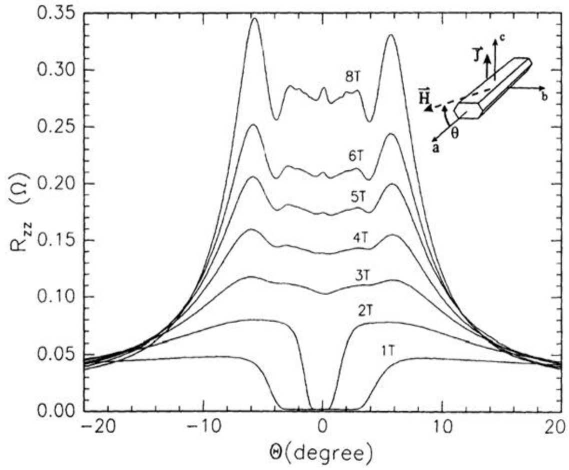

Figure 1.3: The figure shows the oscillation in R_{zz}, when the magnetic field is rotated in the (x, z) plane (Danner-Kang-Chaikin oscillations). The plot was obtained from Ref. [9].

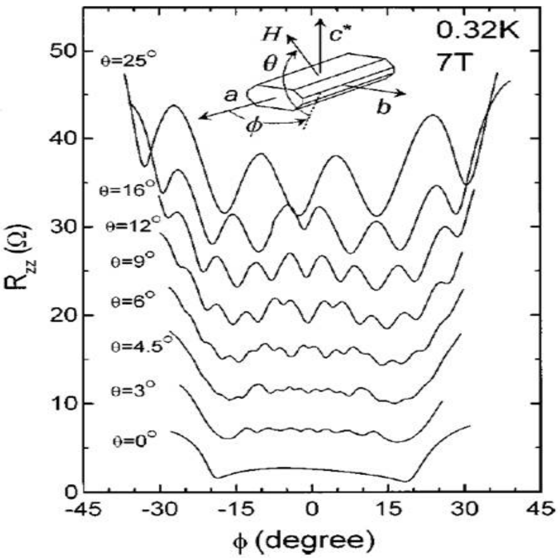

Figure 1.4: The figure shows the oscillation in R_{zz}, when the magnetic field is rotated in the (x, y) plane (Third Angular Effect). The effect is best seen for pure (x, y) rotation $(\theta = 0)$. The plot was obtained from Ref. [14].

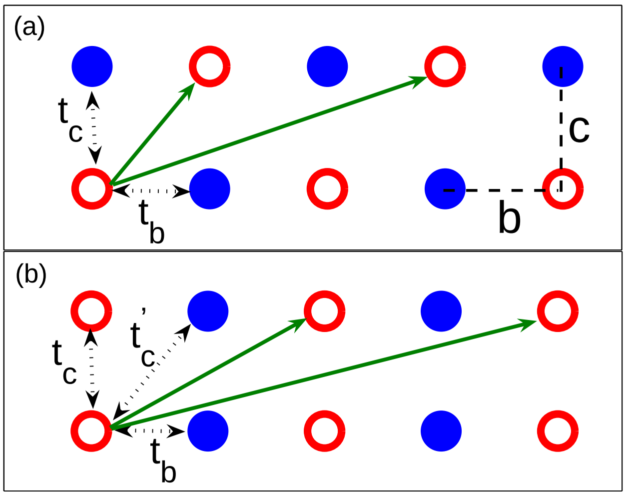

Figure 1.5: A view along the chains of a Q1D metal with the anion ordering at a wave vector $\boldsymbol{Q}$. The filled and open circles represent the chains with the energies $\pm E_g$. (a) (TMTSF)$_2$ReO$_4$, $\boldsymbol{Q} = (0, 1/2, 1/2)$. (b) (TMTSF)$_2ClO_4$, $\boldsymbol{Q} = (0, 1/2, 0)$.

Although initially the different types of AMRO were treated as separate phenomena, a unified picture emerged in recent years due to substantial experimental and theoretical progress. A three-dimensional visualization of the experimentally measured $\sigma_{zz}(\boldsymbol{B})$ [16] demonstrated that the different types of AMRO can be viewed as modulations of the basic Lebed resonances. Measurements with carefully placed electric contacts [17] proved that AMRO exist only in the transverse resistance R_{zz} and not in the longitudinal resistance R_{xx} along the chains. Theory always predicted this difference, but many experiments observed AMRO in R_{xx} as well because of mixing between different components of the conductivity tensor. AMRO were found not only in the dc conductivity, but also in the ac conductivity at microwave frequencies [18, 19]. The ac measurements were interpreted in terms of the so-called period orbit resonance (POR) [20], which is a generalization of cyclotron resonance to more complicated (e.g., open) Fermi surfaces [21]. The ac resonances occur at the angles depending on frequency ω and deviating from Eq. (1.1) [18, 19], so the Lebed magic angles are not truly magic [22, 23]. This observation eliminates theoretical scenarios proposing a radical change in the ground state of the system depending on the magnetic field orientation along the magic or non-magic angles. This conclusion is also supported by the absence of any angular effect in NMR [24].

Given these experimental facts, AMRO most likely represent some sort of a resonance effect in the dc and ac transport coefficients. The first theoretical calculation along these lines was done in Ref. [25] using the Kubo formula with the electron wave functions for a magnetic field in the (y, z) plane. This quantum-mechanical calculation was then generalized to include the B_x component of the magnetic field [26] and the anion superstructure of $(\mathrm{TMTSF})_2\mathrm{ClO}_4$ [27, 28]. In another theoretical approach, the Boltzmann kinetic equation was solved for a constant relaxation time τ by using quasiclassical electron trajectories on the Fermi surface [12, 13, 14, 15, 20, 21, 29, 30, 31, 32]. This solution can be written in a general form using the so-called Shockley tube integral [33] or the Chambers formula [34], see also Ziman's book [35]. In the third theoretical approach, the interlayer conductivity was calculated using a perturbation theory in the electron tunneling amplitude between two layers [36, 37, 38]. In this approach, AMRO originate from Aharonov-Bohm quantum interference in interlayer tunneling in the presence of a magnetic field [38]. All these three seemingly different theoretical approaches produce the same final results and are essentially equivalent.

Interestingly, the model of a Q1D bilayer in a magnetic field [38] is mathematically equivalent to a superconducting qubit driven by an ac electric field and detuned by a dc field [39, 40, 41, 42, 43]. The Mach-Zehnder interference pattern found for the superconducting qubit (the so-called Bessel staircase) [39, 40] is essentially the same as the AMRO pattern in Q1D conductors derived from the Aharonov-Bohm quantum interference [38]. The same equations also describe laser cooling of trapped ions [44]. The similarity in the behavior of these systems demonstrates that quantum coherence in the Q1D organic conductors at low temperatures is as high as in the superconducting qubits and ion traps, which are actively considered for applications in quantum computing and quantum information.

1.2 Personal income distribution

The study of income distribution has a long history. More than a century ago, Pareto [45] proposed that income distribution obeys a universal power law (valid for all time and countries)

$$P(x) \propto Cx^{-\alpha}, \tag{1.2}$$

where $P(x)dx$ is the probability to find income in the interval x, to $x+dx$, α is called the Pareto index, and C is the normalization constant. Subsequent studies found that this conjecture applies only to the top $1\div3\%$ of the population. The question of what is the distribution for the majority ($97\div99\%$) of population with lower incomes remains open. Gibrat [46] proposed that income distribution is governed by a multiplicative random process resulting in the log-normal distribution. However, Kalecki [47] pointed out that such a log-normal distribution is not stationary, because its width keeps increasing with time. Nevertheless, the log-normal function is widely used in literature to fit the lower part of income distribution [48, 49, 50]. Yakovenko and Drăgulescu [51] proposed that the distribution of individual income should follow the exponential law analogous to the Boltzmann-Gibbs distribution of energy in statistical physics. They found substantial evidence for this in the statistical data for USA [52, 53, 54, 55]. Also widely used is the gamma distribution, which differs from the exponential one by a power-law prefactor [56, 57, 58]. For a recent collection of papers discussing these distributions, see the book [59].

1.3 Outline of the Thesis

The outline of the thesis is as follows. In chapter 2 we study the effect of crystal superstructures, produced by orientational ordering of the ReO_4 and ClO_4 anions in the quasi-one-dimensional organic conductors $(TMTSF)_2ReO_4$ and $(TMTSF)_2ClO_4$, on the angular magnetoresistance oscillations (AMRO) observed in these materials.

In chapter 3 we discuss the angular magnetoresistance oscillations in graphene bilayer. We also study the low energy band structure of graphene bilayer in the presence of a parallel magnetic field.

In chapter 4 we analyze the data on individual income from Australia. We fit the data with different functions used to describe distribution of individual income and compare the quality of the fits.

In chapter 5 we analyze data on individual income from IRS and university of Maryland. We also discuss a stochastic model that captures the two-class structure of income distribution is the USA.

Chapter 2

Angular magnetoresistance oscillations in quasi-one-dimensional organic conductors in the presence of a crystal superstructure

Despite substantial progress in understanding of AMRO in Q1D conductors, some experimental results remain unexplained. One open problem is the angular oscillations of the Nernst effect [60]. Another unresolved problem is the angular minimum and saturation of the interlayer resistivity R_{zz} observed for a magnetic field in the y direction [7, 16, 15, 61]. Although the manifestations of AMRO are qualitatively similar in all members of the (TMTSF)$_2$X family, direct comparison of the measurements in (TMTSF)$_2$PF$_6$, (TMTSF)$_2$ClO$_4$, and (TMTSF)$_2$ReO$_4$ shows substantial differences [61].

For a magnetic field rotation in the (y, z) plane with $B_x = 0$, only three strong Lebed peaks in σ_{zz} with $n = 0, \pm 1$ are observed in (TMTSF)$_2$PF$_6$ [7, 61] (see Fig. 1.2). When special care is taken to ensure that $B_x = 0$, the very weak peaks with $n = \pm 2$ in (TMTSF)$_2$PF$_6$ disappear completely [16]. In contrast, in (TMTSF)$_2$ReO$_4$, strong Lebed oscillations are observed up to $n = \pm 11$ [62] (see Fig. 2.1). In (TMTSF)$_2$ClO$_4$, the Lebed oscillations are much weaker in amplitude than in (TMTSF)$_2$PF$_6$ and (TMTSF)$_2$ReO$_4$ [61], but many Lebed resonance can be detected after differentiation of the data with respect to the angle of rotation [4, 5]. The strength of the DKC oscillations is also very different in these materials. The

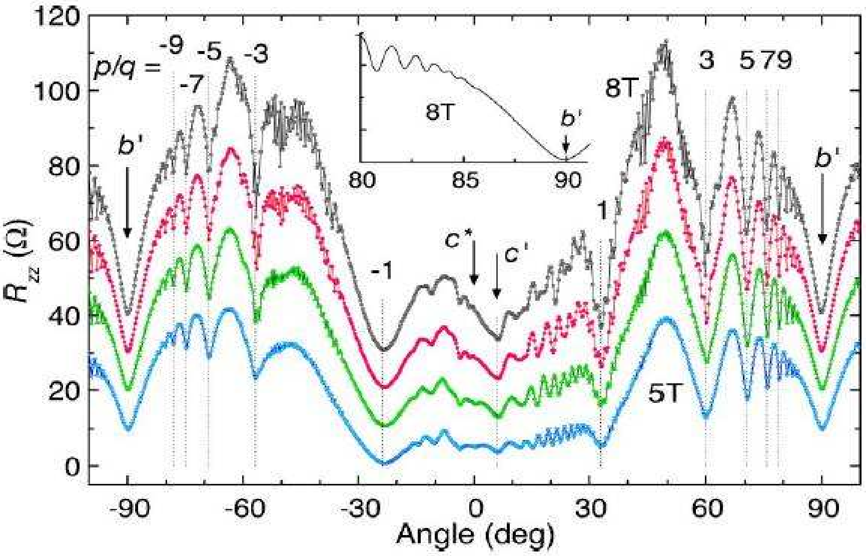

Figure 2.1: Figure shows the AMRO in $(\mathrm{TMTSF})_2\mathrm{ReO}_4$ as a function of the orientation of the magnetic field. For a magnetic field rotation in (y, z) plane, many-strong Lebed oscillations are observed at odd Lebed angles. The plot was obtained from Ref. [62].

DKC oscillations are quite strong in $(\mathrm{TMTSF})_2\mathrm{ClO}_4$, where they were originally discovered [9]. In $(\mathrm{TMTSF})_2\mathrm{PF}_6$, Ref. [10] found very weak DKC oscillations, but Ref. [61] found them to be substantial. However, in $(\mathrm{TMTSF})_2\mathrm{ReO}_4$, the DKC oscillations are extremely weak and almost invisible [61]. This dramatic difference in manifestations of AMRO in the three materials requires a theoretical explanation.

When a magnetic field is rotated in the (y, z) plane at $B_x = 0$, the theoretical calculations cited above show that the Lebed peaks in σ_{zz} can exist only for those magic angles (n, m) where the interchain tunneling amplitudes in the directions $n\boldsymbol{b}+m\boldsymbol{c}$ are present [25, 63]. It is reasonable to expect that the interplane tunneling amplitudes in $(\mathrm{TMTSF})_2\mathrm{PF}_6$ exist between the nearest and next-nearest chains in the $\boldsymbol{c}$ and $\boldsymbol{c} \pm \boldsymbol{b}$ directions (see Fig. 1.5). This would explain why only the Lebed resonance with $n = 0, \pm 1$ are observed in (TMTSF)$_2$PF$_6$. However, many magic angles with big numbers n are observed in (TMTSF)$_2$ClO$_4$ and (TMTSF)$_2$ReO$_4$. It is hard to imagine that direct electron overlap exists between the chains separated by 11 interchain distances.

One way to resolve this problem is to take into account the nonlinear electron dispersion along the chains. (All theoretical papers cited above make a linearized approximation for the electron dispersion along the chains.) The first attempt in this direction was made in Ref. [64], and a more systematic study was presented in Refs. [65, 66]. The nonlinearity can indeed generate an effect similar, albeit not completely equivalent, to presence of many interchain tunneling amplitudes. However, the nonlinearity alone is not sufficient to explain the differences in AMRO between the three compounds. Another problem is the absence of the DKC oscillations in (TMTSF)$_2$ReO$_4$. One might think that quantum coherence is too low in this material, but the existence of 21 Lebed oscillations clearly refutes this idea [62]. We see that a detailed theoretical understanding of AMRO in the (TMTSF)$_2$X materials is challenging and requires additional ideas.

We believe that the key to understanding of the differences in AMRO is the presence of anion ordering in (TMTSF)$_2$ClO$_4$ and (TMTSF)$_2$ReO$_4$ and its absence in (TMTSF)$_2$PF$_6$. PF$_6$ is an octagonal centrosymmetric anion, which does not experience any orientational ordering at low temperatures. In contrast, ClO$_4$ and ReO$_4$ are tetragonal anions without inversion symmetry. Because their crystal sites have inversion symmetry, these anions have two different orientations of the same energy. At low temperatures, the anions experience orientational ordering and produce crystal superstructures [1] with the wave vectors $\boldsymbol{Q} = (0, 1/2, 0)$ in (TMTSF)$_2$ClO$_4$ (under ambient pressure) and $\boldsymbol{Q} = (0, 1/2, 1/2)$ in (TMTSF)$_2$ReO$_4$ (under pressure greater than about 10 kbar), as shown in Fig. 1.5. Formation of a crystal superstructure affects electron spectrum by folding the Brillouin zone. In this chapter, we show that reconstruction of the electron dispersion caused by the anion ordering generates effective tunneling amplitudes between many distant chains. This effect explains why many Lebed angles are observed in (TMTSF)$_2$ReO$_4$ and (TMTSF)$_2$ClO$_4$, but not in (TMTSF)$_2$PF$_6$. It also explains why the magic angles (1.1) are observed only for odd n in (TMTSF)$_2$ReO$_4$ [62] and only for even n in (TMTSF)$_2$ClO$_4$ [4, 5] at $m = 1$. We also explain the differences in the DKC oscillations within the same framework.

In contrast to the previous theories of AMRO for the anion superstructure of (TMTSF)$_2$ClO$_4$ [27, 28, 31, 65], we take into account the direct effect of anion ordering on the interlayer tunneling amplitude, which is especially important for (TMTSF)$_2$ReO$_4$. In this way, we can capture the characteristic features of AMRO in the three compounds without invoking the nonlinearity of the longitudinal electron dispersion [65, 66].

In the second part of this chapter (Sec. 2.5), we study the effect of a strong magnetic field parallel to the layers. We show that, when B_y is strong enough and exceeds a certain threshold related to the anion gap E_g, the interlayer tunneling between different branches of the folded electron dispersion becomes possible, and σ_{zz} should increases sharply. Experimental observation of this effect would allow direct measurement of E_g. This effect can be also applied to study the interband tunneling in κ-(ET)$_2$Cu(NCS)$_2$. A theory of this effect cannot be formulated within the framework of quasiclassical orbits on a warped Fermi surface. We calculate interlayer conductivity in the presence of anion ordering using the quantum limit, where the electron wave functions are confined to the layers due to a strong parallel magnetic field [67, 68, 69, 70].

2.1 Calculation of interlayer conductivity

The general form of the electron dispersion in a Q1D metal is

$$\varepsilon(\boldsymbol{k}) = \pm\hbar v_F(k_x \mp k_F) + \varepsilon_\perp(k_y, k_z), \tag{2.1}$$

where the energy ε is measured from the Fermi energy, and $\boldsymbol{k} = (k_x, k_y, k_z)$ is the electron wave vector. Here we linearize the dispersion along the chains with the Fermi velocity v_F near the Fermi wave vectors $\pm k_F$. There are two sheets of the open Fermi surface, but we present calculations only for the sheet with $+v_F$. Since $t_c \ll t_b$, we can expand the transverse dispersion $\varepsilon_\perp$ to the lowest order in the interlayer tunneling amplitude t_c

$$\varepsilon_\perp(k_y, k_z) = 2t_b\varepsilon_y(k_yb) + 2t_cf(k_yb)\cos(k_zc). \tag{2.2}$$

For a simple model with electron tunneling between the nearest chains in the absence of a superstructure, Eq. (2.2) reduces to the standard tight-binding expression with $\varepsilon_y(k_y) = \cos(k_yb)$ and $f(k_yb) = 1$. However, we will show in Secs. 2.3 and 2.4 that a nontrivial function $f(k_yb)$ appears in the interlayer tunneling term in the presence of anion ordering. This effect was not considered in previous literature and plays crucial role in our consideration.

We calculate the interlayer conductivity by solving the Boltzmann kinetic equation under the relaxation time approximation [35]

$$\frac{\partial g(\boldsymbol{k})}{\partial t} = e\boldsymbol{E} \cdot \boldsymbol{v}(\boldsymbol{k}) \left(-\frac{\partial f^0}{\partial \varepsilon} \right) - \frac{g(\boldsymbol{k})}{\tau}, \tag{2.3}$$

where $g(\boldsymbol{k})$ is the deviation of the local distribution function from the local equilibrium distribution function, e is the electron charge, $\boldsymbol{E}(t) = \mathrm{Re}[\boldsymbol{E}e^{i\omega t}]$ is the applied, time-dependent electric field, f^0 is the Fermi distribution, and τ is a relaxation time. The above equation has the solution

$$g(\boldsymbol{k}(t)) = e \int\limits_{-\infty}^{t} dt' e^{-(t-t'-i\omega)/\tau} \boldsymbol{v}(\boldsymbol{k}^{(t')}) \cdot \boldsymbol{E} \left(-\frac{\partial f^0}{\partial \varepsilon} \right). \tag{2.4}$$

The current density in an energy band is defined as

$$\boldsymbol{J} = e \int \frac{d\boldsymbol{k}}{(2\pi)^3} \boldsymbol{v}(\boldsymbol{k}) g(\boldsymbol{k}). \tag{2.5}$$

Substituting Eq. (2.4) into Eq. (2.5) we get

$$\boldsymbol{J} = 2e^2 \int \frac{d\boldsymbol{k}}{(2\pi)^3} \boldsymbol{v}(\boldsymbol{k}^{(t)}) \int\limits_{-\infty}^{t} dt' e^{-(t-t'-i\omega)/\tau} \left(-\frac{\partial f^0}{\partial \varepsilon} \right) \boldsymbol{v}(\boldsymbol{k}^{(t')}) \cdot \boldsymbol{E}, \tag{2.6}$$

where the factor of 2 comes from the two spin projections. If the temperature is sufficiently low that $T \ll \epsilon_F$, then $-\partial f^0/\partial \varepsilon$ in Eq. can be replaced by $\delta(\varepsilon_F - \varepsilon(\boldsymbol{k}))$, and we get the interlayer conductivity

$$\sigma_{zz} = 2e^2 \int \frac{d\boldsymbol{k}}{(2\pi)^3} v_z(\boldsymbol{k}^{(t)}) \int\limits_{-\infty}^{t} dt' e^{-(t-t'-i\omega)/\tau} v_z(\boldsymbol{k}^{(t')}) \, \delta(\varepsilon_F - \varepsilon(\boldsymbol{k})). \tag{2.7}$$

Since the transverse dispersion $\varepsilon_\perp$ is much smaller than the dispersion along the chain, from Eq. (2.1) we get $\varepsilon(\boldsymbol{k}) \approx \hbar v_F(k_x \pm k_F)$. Substituting this expression in

Eq. (2.7) and integrating with respect to k_x we get the Shockley tube integral [35]

$$\sigma_{zz} = \frac{4e^2}{\hbar} \iint \frac{dk_y^{(0)} dk_z^{(0)}}{(2\pi)^3 v_F} \int\limits_{-\infty}^{0} dt\, v_z(\boldsymbol{k}^{(0)}) v_z(\boldsymbol{k}^{(t)}) e^{t(1/\tau - i\omega)}. \tag{2.8}$$

To obtain the interlayer conductivity from the above formula, we need the time dependence of v_z. From the dispersion relation (2.1), we obtain the electron velocity $\boldsymbol{v} = \partial\varepsilon/\hbar\partial\boldsymbol{k}$

$$v_x = v_F, \quad v_y \approx \frac{2t_b}{\hbar} \frac{d\varepsilon_y}{dk_y}, \quad v_z = -\frac{2t_c c}{\hbar} f(k_y b) \sin(k_z c). \tag{2.9}$$

In the quasiclassical approximation, the time-dependent electron wave vector $\boldsymbol{k}^{(t)}$ follows the equation of motion

$$\hbar \frac{d\boldsymbol{k}^{(t)}}{dt} = e\boldsymbol{v}^{(t)} \times \boldsymbol{B}, \tag{2.10}$$

where e is the electron charge, and the magnetic field $\boldsymbol{B}$ is in the SI units. Given that $v_x = v_F \gg v_z$, we find

$$\frac{dk_y^{(t)}}{dt} \approx -\frac{ev_F B_z}{\hbar}, \; k_y^{(t)} = -\frac{\omega_c t}{b} + k_y^{(0)}, \; \omega_c = \frac{ebv_F B_z}{\hbar}, \tag{2.11}$$

where ω_c is the analog of the cyclotron frequency for the open Fermi surface. The equation of motion for k_z is

$$dk_z = \frac{e}{\hbar}\left(v_F B_y dt - \frac{2t_b B_x}{\hbar} \frac{d\varepsilon_y}{dk_y} dt \right). \tag{2.12}$$

Using $\mathrm{d}k_y/\mathrm{d}t$ from Eq. (2.11), we get

$$ck_z^{(t)} = B_y' \omega_c t + B_x' \varepsilon_y(k_y^{(t)}) + ck_z^{(0)}, \tag{2.13}$$

where we introduced the dimensionless parameters

$$B_y' = \frac{B_y}{B_z} \frac{c}{b}, \quad B_x' = \frac{B_x}{B_z} \frac{2t_b c}{\hbar v_F}. \tag{2.14}$$

The variables B_y' and B_x' are proportional to the tangents of the magnetic field projections onto the (y,z) and (x,z) planes, respectively.

Substituting Eqs. (2.9), (2.11), and (2.13) into Eq. (2.8), we find the real part of σ_{zz}

$$\begin{aligned}\sigma_{zz} = \frac{e^2 t_c^2 c}{\pi^2 \hbar^3 \omega_c v_F b} \mathcal{R}e \sum_{\mp} \int_0^{2\pi} d\phi \int_0^{\infty} d\eta\, f(\phi) f(\phi+\eta) \\ \times \exp\{iB_x'[\varepsilon_y(\phi) - \varepsilon_y(\phi+\eta)] - \eta[1/\omega_c\tau - iB_y' \mp i\omega/\omega_c]\},\end{aligned} \tag{2.15}$$

where $\phi = bk_y^{(0)}$ and $\eta = -\omega_c t$. Expanding the periodic functions $f(\phi)\, e^{iB_x'\varepsilon(\phi)}$ in Eq. (2.15) into the Fourier series with the coefficients

$$A_n(B_x') = \frac{1}{2\pi} \int_0^{2\pi} e^{-in\phi} f(\phi) e^{iB_x'\varepsilon_y(\phi)}\, d\phi, \tag{2.16}$$

we obtain

$$\frac{\sigma_{zz}}{\sigma_0} = \frac{1}{2} \sum_{\mp} \sum_{n=-\infty}^{\infty} \frac{|A_n(B_x')|^2}{1 + (\omega_c\tau)^2 (n - B_y' \mp \omega/\omega_c)^2}. \tag{2.17}$$

Here $\sigma_0 = (4e^2 t_c^2 \tau c)/(\pi \hbar^3 v_F b)$ is the interlayer dc conductivity at $\boldsymbol{B} = 0$, and the ± terms represent contributions from the two sheets of the Fermi surface. In the rest of the chapter, we shall focus on the dc conductivity σ_{zz} at $\omega = 0$, although Eq. (2.17) also gives the ac conductivity.

The Lebed effect corresponds to the resonant peaks of σ_{zz} in Eq. (2.17) achieved at $B_y' = n$, where the condition (1.1) for $m = 1$ is satisfied. In a simple model without anion ordering, where $\varepsilon_y = \cos(k_y b)$ and $f = 1$, Eq. (2.16) reduces to $A_n(B_x') = i^n J_n(B_x')$, where J_n is the Bessel function. In this case, Eq. (3.7) reproduces the result found in Refs. [38, 36, 37, 26, 32]. However, the coefficients $J_n(B_x')$ vanish for $n \neq 0$ at $B_x = 0$, so there are no Lebed oscillations in this model for a magnetic field rotation in the (y, z) plane. The DKC effect originates from the oscillations of $J_n(B'_x)$ vs. B'_x in the numerator of Eq. (2.17).

Interestingly, Eq. (2.17) with $|A_n|^2 = J_n^2(B'_x)$ and $\omega = 0$ is exactly the same as the equation that describes the Mach-Zehnder interference in a superconducting qubit driven by an ac electric field and subjected to a dc bias [39, 40]. The two states of the qubit correspond to the two adjacent layers of a Q1D conductor coupled by the tunneling amplitude t_c. The frequency of the ac field for the qubit maps to the frequency ω_c in Eq. (2.11), the detuning of the qubit maps to $B'_y\omega_c = ecv_F B_y/\hbar$, and the amplitude of the ac modulation maps to B'_x in Eq. (2.14). The contour plot of Eq. (2.17) shown in Fig. 2 of Ref. [38] is exactly the same as in Refs. [39, 40] and represents the so-called Bessel staircase. The same equation also appears in the theory of laser cooling in ion traps [44]. This correspondence is not just a mathematical curiosity, but reflects profound similarity between these highly coherent quantum system, where the oscillatory patterns are caused by phase interference due to applied electric and magnetic fields.

2.2 Interlayer conductivity in $\mathbf{(TMTSF)_2PF_6}$ without anion ordering

Let us first discuss the case of $(\mathrm{TMTSF})_2\mathrm{PF}_6$, which does not have anion ordering. In order to observe more than one Lebed angle, we need to introduce the tunneling amplitude t'_c between next-nearest neighboring chains, as shown in Fig. 1.5(b).

Including this term in the transverse dispersion (2.2), we find for $(\mathrm{TMTSF})_2\mathrm{PF}_6$

$$\varepsilon_y(\phi) = \cos\phi, \quad f(\phi) = 1 + 2\frac{t_c'}{t_c}\cos\phi, \quad \phi = bk_y. \tag{2.18}$$

In a more general case, where the amplitudes t_n corresponding to the tunneling vectors $\boldsymbol{c} + n\boldsymbol{b}$ are present, the transverse dispersion relation can be written as

$$\varepsilon_\perp(k_y, k_z) = 2t_b\cos(k_y b) + 2\sum_l t_l \cos(k_z c + l k_y b). \tag{2.19}$$

Eq. (2.18) is the special case of Eq. (2.19) with $t_0 = t_c$ and $t_{\pm 1} = t_c'$.

Generalizing the derivation presented in Sec. 2.1 to the transverse dispersion relation (2.19), we find that the interlayer conductivity σ_{zz} is given by Eq. (2.17) with the following coefficients A_n [71]

$$A_n(B_x') = \frac{1}{t_c}\sum_l i^{n+l} t_l J_{n+l}(B_x'). \tag{2.20}$$

In the case of $(\mathrm{TMTSF})_2\mathrm{PF}_6$, Eqs. (2.16) and (2.18) or Eq. (2.20) give

$$A_n(B_x') = i^n J_n(B_x') + i^{n+1}\frac{t_c'}{t_c}J_{n+1}(B_x') + i^{n-l}\frac{t_c'}{t_c}J_{n-1}(B_x'). \tag{2.21}$$

Substituting Eq. (2.21) into Eq. (3.7), we find the following results for AMRO in $(\mathrm{TMTSF})_2\mathrm{PF}_6$:

When $B_x' = 0$, i.e. we consider a magnetic field rotation in the $(y.z)$ plane, only the terms with $n = 0$ and $n = \pm 1$ have non-zero coefficients A_n in the sum in Eq. (3.7). These terms give rise to the Lebed peaks at $n = 0$ and $n = \pm 1$ with the heights proportional to t_c^2 and $(t_c')^2$.

When we consider the DKC oscillations at $B_y' = 0$, i.e. for a magnetic field rotation in the $(x.z)$ plane, the sum in Eq. (2.17) is dominated by the term with

$n = 0$, because the other terms have the big factor $(\omega_c \tau)^2$ in the denominator. Keeping only the term with $n = 0$ and using Eq. (2.21), we can write approximately

$$\frac{\sigma_{zz}(B'_x)}{\sigma_0} \approx \left| J_0(B'_x) + 2i\frac{t'_c}{t_c} J_1(B'_x) \right|^2 . \tag{2.22}$$

When $t'_c = 0$, Eq. (2.22) vanishes for the angles where $J_0(B'_x) = 0$, which is a manifestation of the DKC oscillations. However, in the presence of $t'_c \neq 0$, Eq. (2.22) does not vanish for any angles, so the DKC oscillations are partially suppressed, although some modulation of σ_{zz} vs. B'_x remains. We see that the presence of tunneling amplitudes t_l to more distant chains enhances the Lebed oscillations, but suppresses the DKC oscillations. This conclusion was already made in Ref. [38].

2.3 Anion ordering in (TMTSF)$_2$ReO$_4$

The ReO$_4$ anions order with the wave vector $\boldsymbol{Q} = (0, 1/2, 1/2)$ under pressure. This causes the energies of the odd and even chains to split by $\pm E_g$, as illustrated in Fig. 1.5(a). The Hamiltonian of interchain tunneling is described by a 2 × 2 matrix representing the even and odd chains [72]:

$$H_\perp = \begin{pmatrix} E_g & 2t_b \cos(k_y b) + 2t_c \cos(k_z c) \\ \text{c.c.} & -E_g \end{pmatrix} . \tag{2.23}$$

The eigenvalues of the matrix (2.23) give the transverse electron dispersion relation

$$\varepsilon_\perp = \pm\sqrt{[2t_b \cos(k_y b) + 2t_c \cos(k_z c)]^2 + E_g^2}. \tag{2.24}$$

Expanding Eq. (2.24) to the zeroth and first order in t_c, we find the functions $\varepsilon_y(k_y)$ and $f(k_y)$ in Eq. (2.2)

$$\varepsilon_y(\phi) \;=\; \pm\sqrt{\cos^2\phi + (E_g/2t_b)^2}, \quad \phi = bk_y, \tag{2.25}$$

$$f(\phi) \;=\; \pm\frac{\cos\phi}{\sqrt{\cos^2\phi+(E_g/2t_b)^2}}. \tag{2.26}$$

The function $f(\phi)$ (2.26) is close to a square wave for $E_g/t_b \ll 1$, as shown in Fig. 2.2(a). Its Fourier coefficients A_n, given by Eq. (2.16) with $B_x' = 0$, are non-zero only for odd n and decay as $1/n$. Transforming Eq. (2.2) from the momentum space to the real space, we find that the Fourier coefficients of $f(k_y b)$ generate effective interplane tunneling amplitudes along the vectors $\boldsymbol{c}+n\boldsymbol{b}$ with odd n, which are shown in Fig. 1.5(a) by the arrows. Initially, the model has only the tunneling amplitudes t_b and t_c between the nearest chains, but the anion ordering generates effective tunneling amplitudes between many chains. The higher-order expansion of Eq. (2.24) in t_c would generate effective tunneling amplitudes along the vectors $m\boldsymbol{c}+n\boldsymbol{b}$ with m and n of the same parity between the sites of the same type, either open circles or closed circles in Fig. 1.5(a). However, one should keep in mind that this heuristic real-space picture [62] is an oversimplification, and an accurate calculation in the momentum space should be performed as described above. In Fig. 2.3 we show the normalized dc conductivity calculated from Eq. (2.17) for $B_x' = 0$ and $\omega_c\tau = \sqrt{50}$ using the Fourier coefficients A_n from Eq. (2.16). Since $A_n \neq 0$ only for odd n, therefore σ_{zz} has peaks only at the odd Lebed angles. as shown in Fig. 2.3 and observed in $(\mathrm{TMTSF})_2\mathrm{ReO}_4$ [62]. The higher-order expansion of Eq. (2.24) in t_c would generate peaks at the Lebed magic angles with m and n of the same parity in Eq. (1.1), as observed in Ref. [62]. Because of the anion superstructure, Eq. (2.24) is highly non-linear in $\cos\phi$, so its Fourier expansion generates a big number of harmonics, which produce a big number of Lebed peaks in AMRO. This

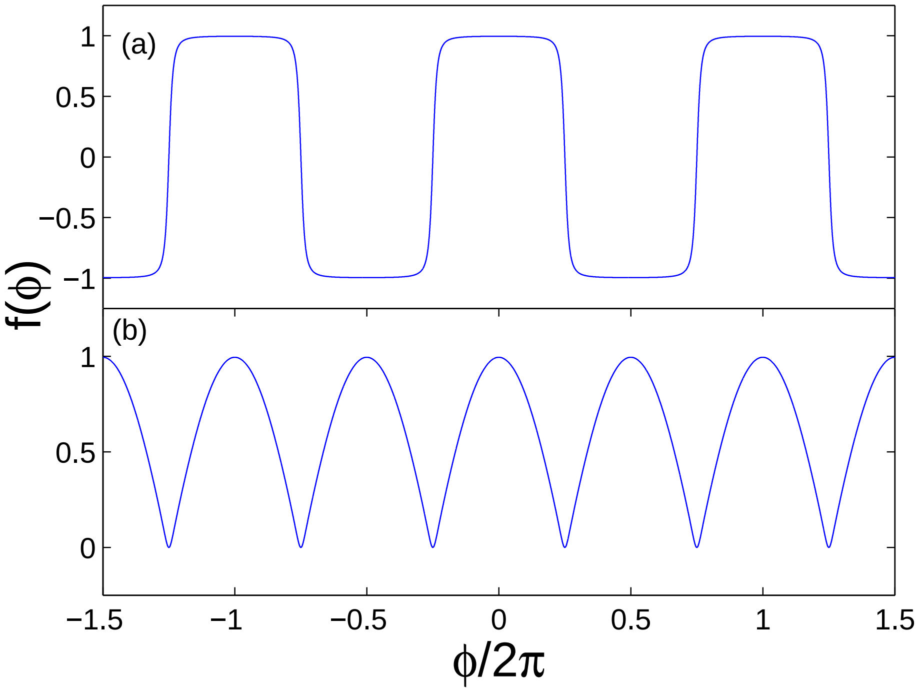

Figure 2.2: (a) Plot of the function $f(\phi)$ given by Eq. (2.26). (b) Plot of the second term in $f(\phi)$ given by Eq. (2.29). In both plots, $E_g/2t_b = 0.1$.

is the qualitative reason why so many Lebed peaks are observed in $(\mathrm{TMTSF})_2\mathrm{ReO}_4$, in contrast to $(\mathrm{TMTSF})_2\mathrm{PF}_6$, which has no anion superstructure.

Fig. 2.4 shows a contour plot of $\ln(\sigma_{zz}/\sigma_0)$ vs. B'_x and B'_y, as calculated from Eq. (3.7) using Eqs. (2.16), (2.25), and (2.26). The conductivity is maximal at the vertical lines corresponding to the odd Lebed magic angles. At a fixed Lebed angle, the weak modulation of σ_{zz} vs. B'_x (along a vertical line) corresponds to the DKC oscillations. Fig. 2.4 shows that the DKC oscillations are very weak, because the coefficients $A_n(B'_x)$ (2.16) do not have zeros vs. B'_x in the presence of anion ordering, unlike the Bessel functions $J_n(B'_x)$ in a simple model. This is a theoretical

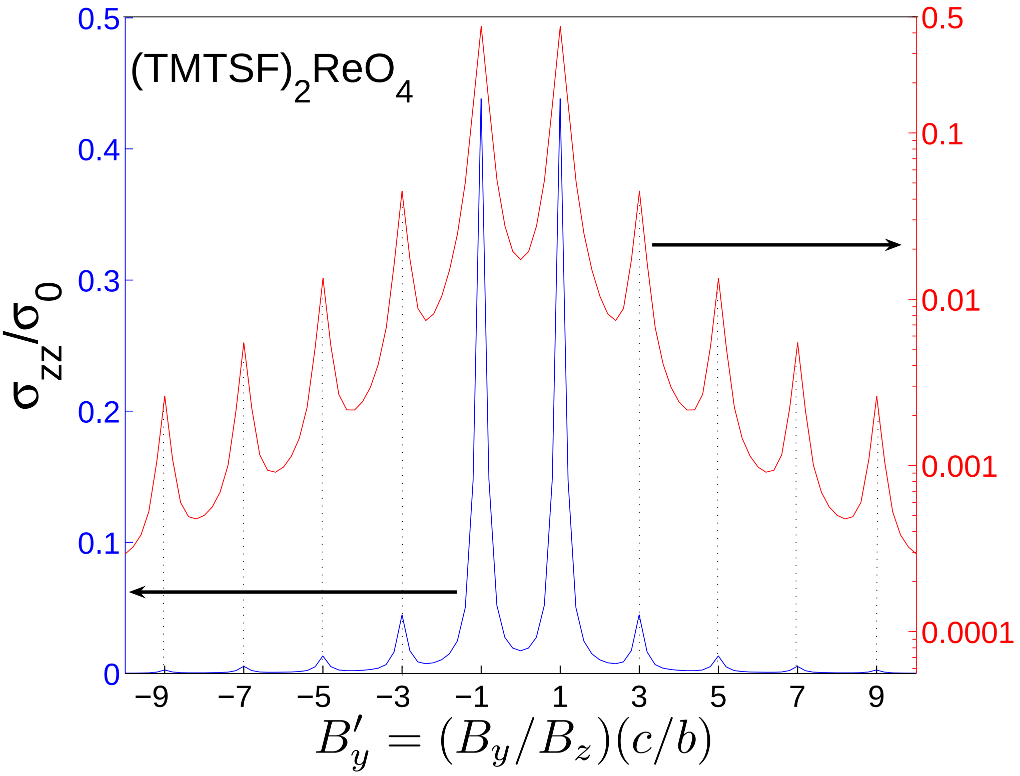

Figure 2.3: Normalized interlayer conductivity σ_{zz}/σ_0 calculated from Eq. (2.17) for (TMTSF)$_2$ReO$_4$ and plotted vs. B'_y at $B'_x = 0$, shown in the linear (left) and logarithmic (right) scales.

explanation of why the DKC oscillations in (TMTSF)$_2$ReO$_4$ are very weak and barely detectable experimentally [62].

2.4 Anion ordering in (TMTSF)$_2$ClO$_4$

In the case of (TMTSF)$_2$ClO$_4$, in order to observe multiple Lebed angles, we need to take into account the tunneling amplitude t'_c introduced in Sec. 2.2 and shown in Fig. 1.5(b). For the anion ordering with $\boldsymbol{Q} = (0, 1/2, 0)$, the interchain tunneling is

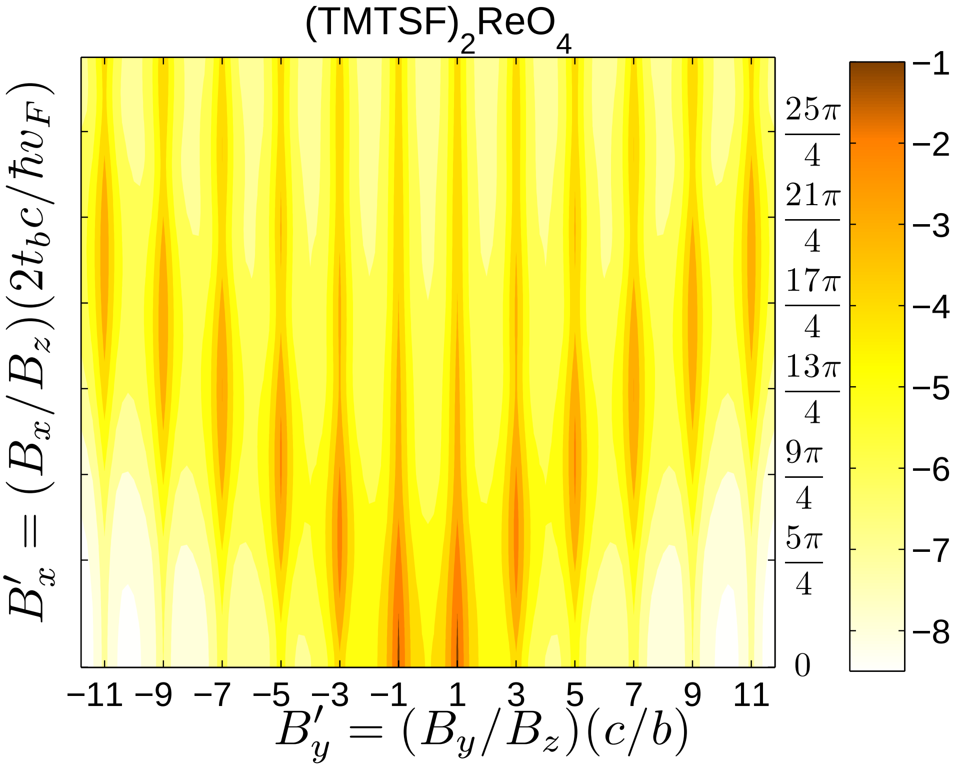

Figure 2.4: Contour plot of $\ln(\sigma_{zz}/\sigma_0)$ calculated from Eq. (2.17) for (TMTSF)$_2$ReO$_4$ at $\omega_c\tau = \sqrt{50}$.

described by the Hamiltonian

$$H_\perp = \begin{pmatrix} E_g + 2t_c\cos(k_z c) & \cos(k_y b)[2t_b + 4t'_c\cos(k_z c)] \\ \text{c.c.} & -E_g + 2t_c\cos(k_z c) \end{pmatrix}. \tag{2.27}$$

The eigenvalues of the matrix (2.27) give the transverse electron dispersion relation

$$\varepsilon_\perp = 2t_c\cos(k_z c) \pm \sqrt{\cos^2(k_y b)[2t_b + 4t'_c\cos(k_z c)]^2 + E_g^2}. \tag{2.28}$$

Expanding Eq. (2.28) to the zeroth and first order in t_c and comparing with Eq. (2.2), we find $\varepsilon_y(\phi)$ to be the same as in Eq. (2.25) and

$$f(\phi) = 1 \pm \frac{t'_c}{t_c}\frac{2\cos^2\phi}{\sqrt{\cos^2\phi + (E_g/2t_b)^2}}. \tag{2.29}$$

Only the second term in Eq. (2.29) generates the coefficients A_n with $n \neq 0$ when substituted into Eq. (2.16) at $B_x = 0$. For $E_g/t_b \ll 1$, this term is close to a rectified cosine signal, as shown in Fig. 2.2(b), and its Fourier coefficients decay as $1/n^2$ for large n. It has non-zero Fourier coefficients only for even n, thus σ_{zz} vs. B'_y has peaks at the even Lebed angles, as shown in Fig. 2.5 for $B'_x = 0$ and observed experimentally in (TMTSF)$_2$ClO$_4$ [4, 5]. Because the second term in Eq. (2.29) is highly nonlinear in $\cos\phi$, it generates many harmonics and many Lebed peaks. However, they decay with the increase of n faster in (TMTSF)$_2$ClO$_4$ than in (TMTSF)$_2$ReO$_4$. Moreover, because t'_c is small, the Lebed oscillations in (TMTSF)$_2$ClO$_4$ are weak, in agreement with the observations in Refs. [4, 5, 61]. As discussed in Sec. 2.2, the DKC oscillations are controlled by the coefficient $A_0(B'_x)$ in Eq. (2.17). The first term in Eq. (2.29) gives the main contribution to $A_0(B'_x)$, proportional to $J_0(B'_x)$. Thus, the DKC oscillations are relatively strong in (TMTSF)$_2$ClO$_4$, as observed in Refs. [9, 61], although they are somewhat reduced by the second term in Eq. (2.29).

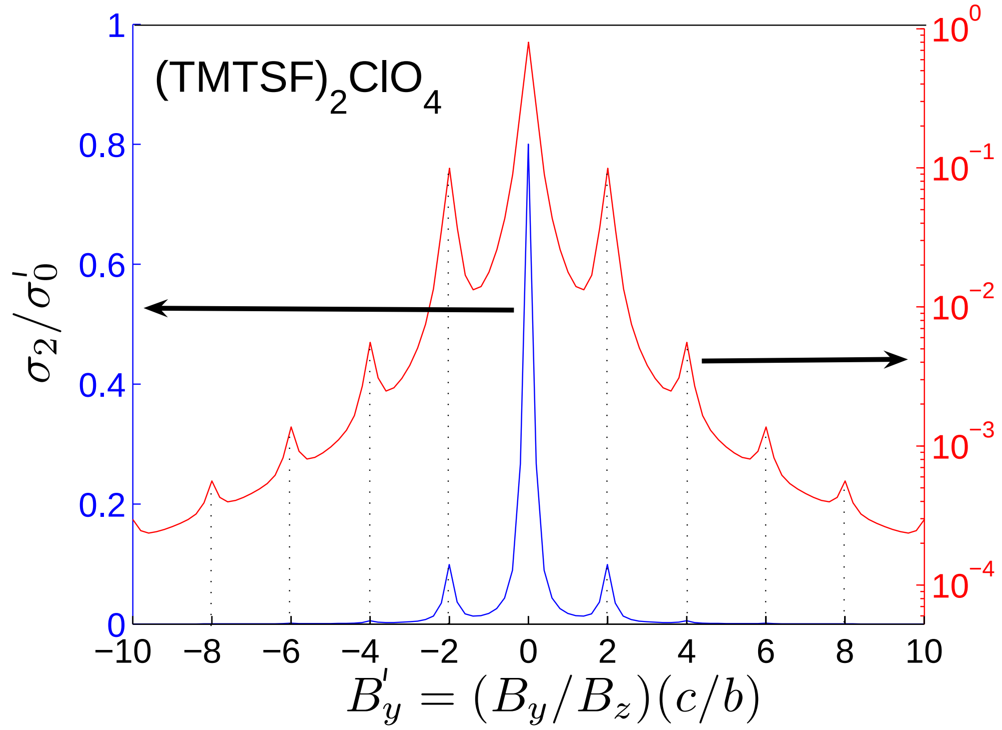

Figure 2.5: Plot of σ_2/σ_0' vs. B_y' at $B_x' = 0$, shown in the linear (left) and logarithmic (right) scales. σ_2 is the contribution to σ_{zz} in Eq. (2.17) from the second term in Eq. (2.29), and $\sigma_0' = \sigma_0(t_c'/t_c)^2$.

We conclude that the different types of anion ordering in (TMTSF)$_2$ReO$_4$ and (TMTSF)$_2$ClO$_4$ can indeed explain the characteristic features of AMRO in these materials. In (TMTSF)$_2$ReO$_4$, the Lebed oscillations are strong and numerous, but the DKC oscillations are very weak. In (TMTSF)$_2$ClO$_4$, the Lebed oscillations are numerous, but weak, whereas the DKC oscillations are relatively strong. On the other hand, there is no anion superstructure in (TMTSF)$_2$PF$_6$. This material exhibits a few, but strong, Lebed oscillations and partially suppressed DKC oscillations.

2.5 Interband tunneling in a strong magnetic field parallel to the layers

Folding of the Brillouin zone due to anion ordering produces two branches (or two bands) of the electron dispersion, which we label by the index $\alpha = \pm$ according to the sign in Eq. (2.25). The Fermi surfaces of the two bands, obtained from Eq. (2.1), are shown by the two solid lines in Fig. 2.6 for $E_g/t_b = 0.1$. (This picture is for the Fermi surface sheets near $+k_F$.)

In this section, we study interlayer conductivity in a strong magnetic field $(B_x, B_y, 0)$ parallel to the layers. We use the formalism developed in Refs. [36, 37, 38] and calculate σ_{zz} between just two layers, i.e. for a bilayer. Assuming that t_c is very weak, one can argue that, in the lowest order in t_c, the interlayer conductivity of a bulk multilayer crystal is determined by the interlayer conductivity between a pair of layers [72].

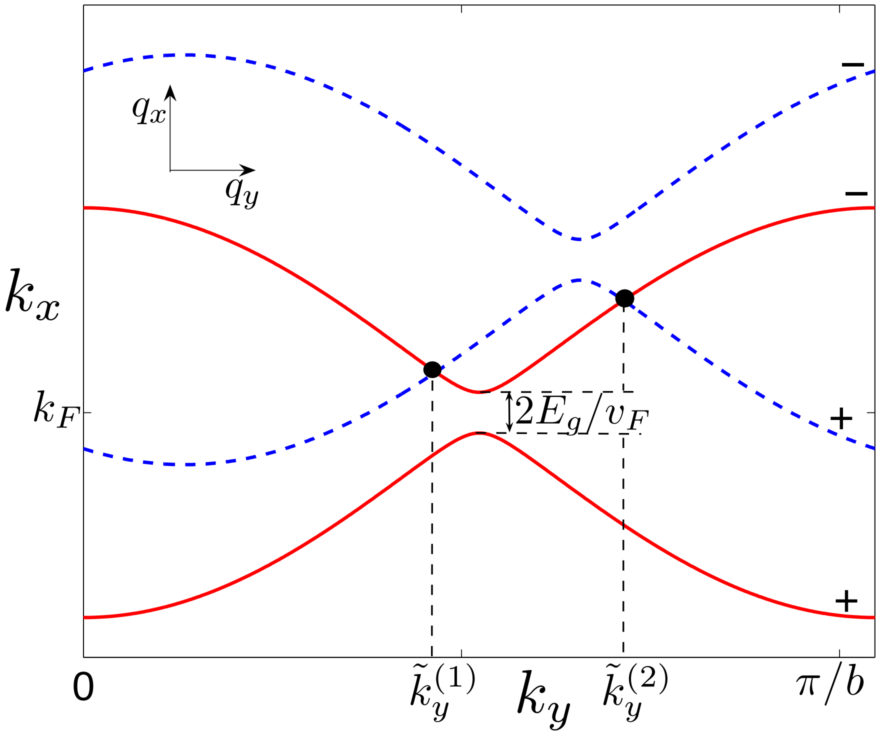

Figure 2.6: Fermi surfaces of two adjacent layers shifted by the vector $\boldsymbol{q}$ of Eq. (2.32) due to an in-plane magnetic field. The Fermi surfaces for each layer (the solid lines and the dashed lines) consist of two bands separated by the gap $2E_g/v_F$ due to anion ordering and labeled + and −.

The tunneling Hamiltonian between layers 1 and 2 is

$$\hat{H}_c = t_c \int \hat{\psi}_2^\dagger(\boldsymbol{r})\,\hat{\psi}_1(\boldsymbol{r})\,e^{i\chi(\boldsymbol{r})} d^2r \; + \text{H.c.}, \tag{2.30}$$

$$\chi(\boldsymbol{r}) = \frac{ec}{\hbar} A_z(\boldsymbol{r}), \quad A_z(\boldsymbol{r}) = B_x y - B_y x, \tag{2.31}$$

where $\hat{\psi}_{1,2}$ are the electron destruction operators in the layers 1 and 2. Here A_z is the vector potential of the in-plane magnetic field, and $\chi(r)$ is the corresponding gauge phase accumulated in the process of tunneling across the interlayer spacing c. Substituting Eq. (2.31) into Eq. (2.30) and using momentum representation in the (x, y) plane, we observe that the in-plane wave vector of the electron changes from $\boldsymbol{k}$ to $\boldsymbol{k}+\boldsymbol{q}$ in the process of tunneling [38], where the vector $\boldsymbol{q}$ is

$$\boldsymbol{q} = (q_x, q_y) = \frac{ec}{\hbar}\,(B_y, -B_x). \tag{2.32}$$

Thus, the Fermi surfaces of the second layer are shifted by the vector $\boldsymbol{q}$ relative to the Fermi surfaces of the first layer as shown by the two dashed lines in Fig. 2.6. A similar picture was discussed for closed Fermi surfaces in semiconducting bilayers in Refs. [36, 73, 74, 75].

The interlayer conductivity $\sigma_{zz}^{\alpha\beta}$ between the bands α and β is given by the following expression [36, 76]

$$\sigma_{zz}^{\alpha\beta} = \frac{e^2 t_c^2 c}{\hbar\pi} \sum_{\boldsymbol{k}} |M_{\alpha\beta}|^2 S(\boldsymbol{k}, E_F) S(\boldsymbol{k}+\boldsymbol{q}, E_F), \tag{2.33}$$

where $M_{\alpha\beta} = \langle \psi_\alpha^{(2)}(\boldsymbol{k}+\boldsymbol{q}) | \psi_\beta^{(1)}(\boldsymbol{k}) \rangle$ is the scalar product between the in-plane electron wave functions belonging to adjacent layers. These matrix elements are discussed in more detail in Appendix 2.7. The total interlayer conductivity is the sum over all bands $\sigma_{zz} = \sum_{\alpha\beta} \sigma_{zz}^{\alpha\beta}$. The function $S(\boldsymbol{k}, E_F)$ is the spectral density of the in-plane electron Green function evaluated at the Fermi energy E_F as a function of the wave vector $\boldsymbol{k}$ [36, 76]

$$S(\boldsymbol{k}, E_F) = \frac{2\Gamma}{[E_F - \varepsilon(\boldsymbol{k})]^2 + \Gamma^2}, \tag{2.34}$$

where $\Gamma = \hbar/2\tau$ is the relaxation rate, and $\varepsilon(\boldsymbol{k})$ is the electron dispersion within the layer.

When Γ is small, i.e., when the electron quasiparticles have a long lifetime time τ, the spectral function (2.34) can be replaced by a delta function: $S(\boldsymbol{k}, E_F) \approx 2\pi\delta[E_F - \varepsilon(\boldsymbol{k})]$. Substituting this expression into Eq. (2.33), we find

$$\begin{aligned} \sigma_{zz}^{\alpha\beta} &= \frac{e^2 t_c^2 c |\tilde{M}_{\alpha\beta}|^2}{\hbar\pi} \iint dk_y\, dk_x\, \delta[\hbar v_F k_x + \alpha 2 t_b \varepsilon_y(k_y b)] \\ &\times \delta[\hbar v_F (k_x - q_x) + \beta 2 t_b \varepsilon_y(k_y b - q_y b)], \end{aligned} \tag{2.35}$$

where the matrix element $\tilde{M}_{\alpha\beta}$ is evaluated at the points where both delta functions are satisfied. Integrating Eq. (2.35) over k_x, we find

$$\sigma_{zz}^{\alpha\beta} = \frac{e^2 t_c^2 c |\tilde{M}_{\alpha\beta}|^2}{\pi\hbar^2 v_F} \int dk_y\, \delta[g_{\alpha\beta}(k_y)], \tag{2.36}$$

where the function $g_{\alpha\beta}(k_y)$ is

$$g_{\alpha\beta}(k_y) = \hbar v_F q_x + 2t_b[\alpha\varepsilon_y(k_y b) - \beta\varepsilon_y(k_y b - q_y b)]. \tag{2.37}$$

Taking the integral (2.36), we find

$$\sigma_{zz}^{\alpha\beta} = \frac{e^2 t_c^2 c}{\pi\hbar^2 v_F} \sum_{\tilde{k}_y} \frac{|M_{\alpha\beta}(\tilde{k}_y)|^2}{|\partial g_{\alpha\beta}/\partial k_y|}, \tag{2.38}$$

where the sum is taken over the points $\tilde{k}_y$ where the equation $g_{\alpha\beta}(\tilde{k}_y) = 0$ is satisfied. Notice that the relaxation time τ drops out from Eq. (2.38), so σ_{zz} should be temperature-independent in a strong parallel magnetic field [36].

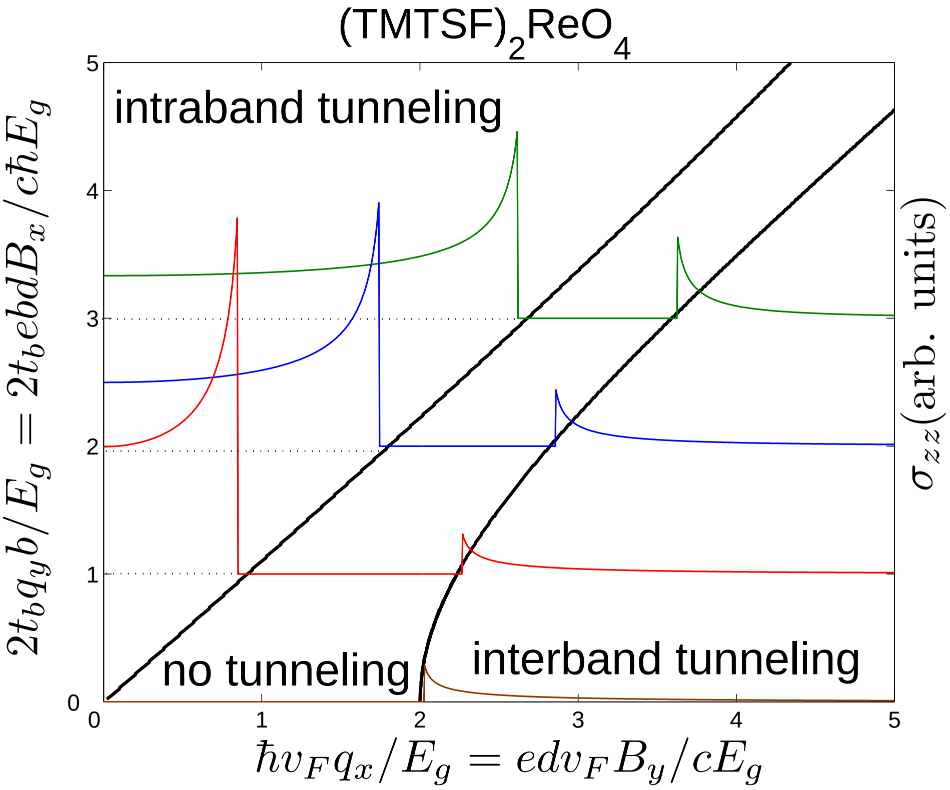

Figure 2.7: Phase diagram of interlayer tunneling vs. the normalized in-plane magnetic field components B_y nd B_x. Tunneling between the same and different types of bands is possible in the upper left and the lower right regions of the diagram, correspondingly, and not possible in the intermediate region. The thin curves show the interlayer conductivity σ_{zz} calculated using Eq. (2.38) as a function of B_y for several values of B_x for the superstructure of (TMTSF)$_2$ReO$_4$.

Eq. (2.35) shows that a non-zero contribution to interlayer conductivity comes from the points where both delta functions are satisfied, i.e., the initial and final states belong to the Fermi surfaces of different layers. Geometrically, these are the intersection points $\tilde{k}_y^{(1)}$ and $\tilde{k}_y^{(2)}$ of the solid and dashed lines in Fig. 2.6. Depending on which Fermi surfaces intersect in Fig. 2.6, electrons can tunnel between different bands $\alpha, \beta = \pm$ in the folded Brillouin zone. The equation $g_{\alpha\beta}(\tilde{k}_y) = 0$ has solutions only in some regions of the (q_x, q_y) space, as shown by the thick solid lines in Figs. 2.7 and 2.8. Above the diagonal line in Figs. 2.7 and 2.8, the interlayer tunneling is possible only between the bands of the same type $\alpha = \beta$. If q_x exceeds the threshold value

$$\hbar v_F q_x = B_y e c v_F \geq 2E_g, \tag{2.39}$$

the interlayer tunneling between different bands, $\alpha = -\beta$, becomes possible in the lower right region in Figs. 2.7 and 2.8. No interlayer tunneling is possible in the intermediate region in Figs. 2.7 and 2.8, where the shifted Fermi surfaces in Fig. 2.6 do not cross. The boundaries of the regions are determined by the condition that the displaced Fermi surface touches the other one.

The plots of the interlayer conductivity σ_{zz}, calculated from Eq. (2.38), are shown in Figs. 2.7 and 2.8 as functions of $B_y \propto q_x$ for several fixed values of $B_x \propto q_y$. We observe that the interlayer conductivity vanishes in the intermediate region and has peaks at the boundaries. The peaks originate from the increase of the phase volume in the integral (2.35) when the two Fermi surfaces touch each other. Fig. 2.7 corresponds to the anion superstructure of $(\mathrm{TMTSF})_2\mathrm{ReO}_4$. We observe that, when

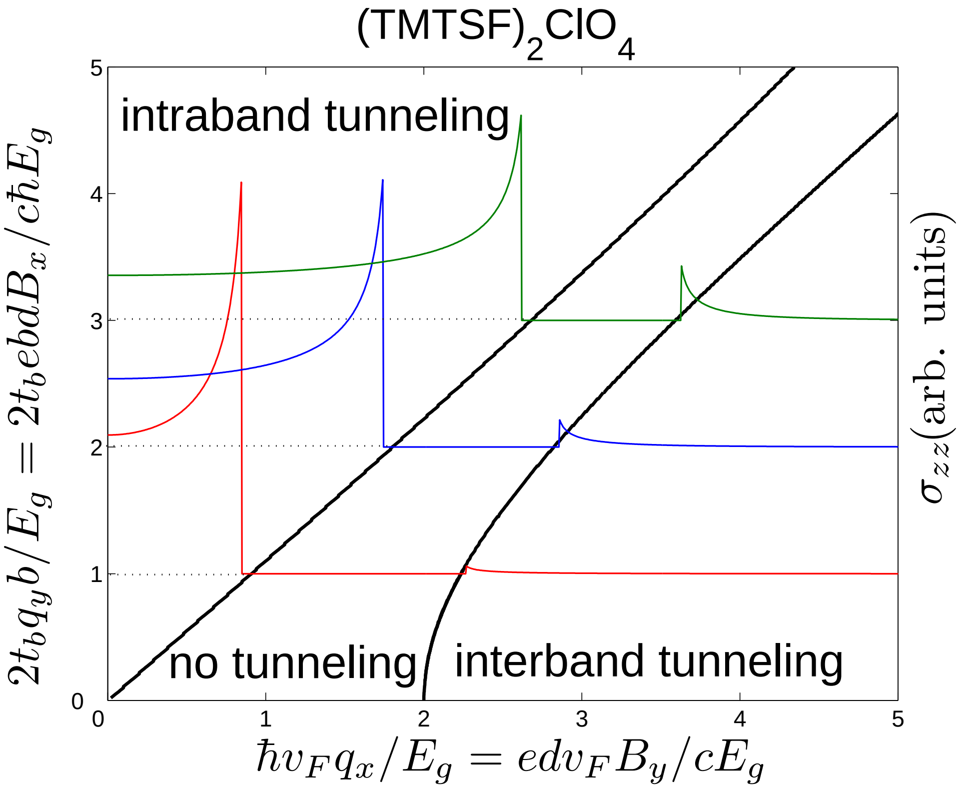

Figure 2.8: The same as in Fig. 2.7, but for the superstructure of (TMTSF)$_2$ClO$_4$.

the magnetic field is applied along the y axis ($B_x = 0$), the interlayer conductivity $\sigma_{zz}(B_y)$ is strongly suppressed until B_y exceeds the threshold, and then σ_{zz} increases sharply. The value of E_g can be determined from the measured threshold field B_y via Eq. (2.39). Fig. 2.8 corresponds to the anion superstructure of (TMTSF)$_2$ClO$_4$. In this case, the eigenfunctions of different bands $\alpha = -\beta$ are orthogonal, so the matrix element M_{-+} vanishes for $q_y = 0$ (see Appendix 2.7). Thus, in order to get a nonzero interlayer conductivity in (TMTSF)$_2$ClO$_4$, it is necessary to have a non-zero component $B_x \neq 0$, so that $q_y \neq 0$.

According to the measurements in Ref. [19], the Fermi velocity in (TMTSF)$_2$ClO$_4$ is $v_F \approx 10^5$ m/s. Substituting this value and the interlayer distance $c = 1.35$ nm [1] into Eq. (2.39) and using the maximal stationary field of 45 T available at NHMFL in Tallahassee, we find the maximal anion gap $2E_g \approx 70$ K that can be probed using this method. Various estimates of E_g are reviewed in Ref. [77]. Refs. [28, 78] estimated E_g as $40 \div 50$ K, so the field of 45 T may be sufficient to exceed the threshold (2.39) at the ambient pressure. The experiment can be also performed in pulsed fields or under pressure, where the anion superstructure is progressively suppressed [79]. Measurements of the interlayer conductivity using pulsed magnetic fields of 46 T were performed in (TMTSF)$_2$ClO$_4$ [80], but the field was applied close to the x axis, rather than the y axis, as required for our effect.

A similar analysis can be also applied to the material κ-(ET)$_2$Cu(NCS)$_2$, whose in-plane Fermi surface is shown in Fig. 2.9. The separation Δk between the α and β branches of the Fermi surface can be measured by applying an in-plane magnetic field in the horizontal direction in Fig. 2.9. This field shifts the Fermi surface of one

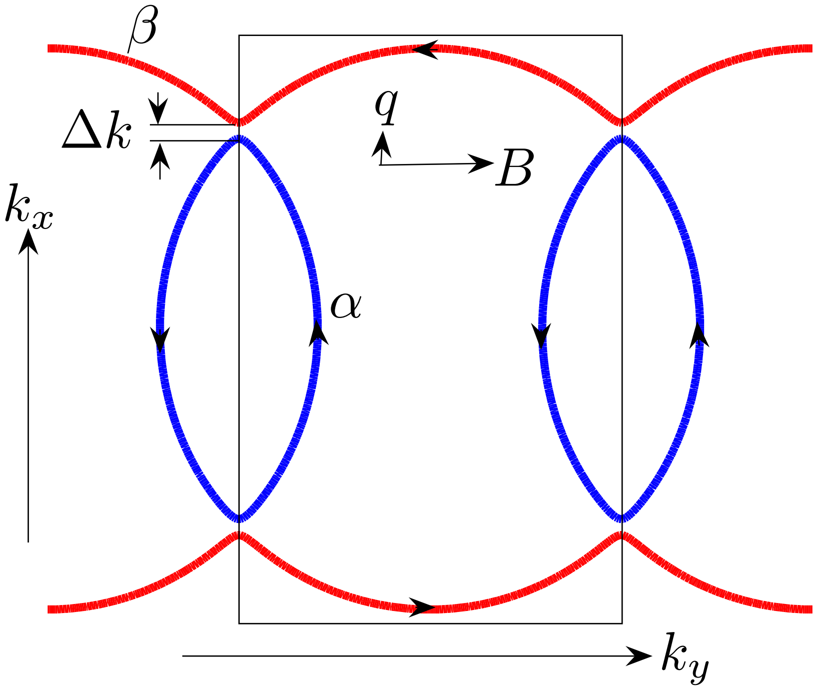

Figure 2.9: The in-plane Fermi surface of κ-(ET)$_2$Cu(NCS)$_2$. The α and β branches of the Fermi surface are separated by the distance Δk in the momentum space.

layer by the vector $\boldsymbol{q}$ shown in Fig. 2.9. The threshold magnetic field, at which the α branch in one layer starts to touch the β branch in the other layer, can be calculated from Eq. (2.32). Using $\Delta k = 0.17$ nm^{-1} and the interlayer distance $c = 1.62$ nm [1, 81], we estimate that the threshold magnetic field is of the order of 430 T, which is beyond the current experimental capabilities.

2.6 Conclusions

We have shown that the modifications of the electron dispersion due to the anion ordering in (TMTSF)$_2$ReO$_4$ and (TMTSF)$_2$ClO$_4$ generate effective tunneling amplitudes between many distant chains. These amplitudes cause peaks in the interlayer conductivity σ_{zz} at many Lebed magic angles (1.1). The different wave vectors of the anion ordering, $\boldsymbol{Q} = (0, 1/2, 1/2)$ in (TMTSF)$_2$ReO$_4$ and $\boldsymbol{Q} = (0, 1/2, 0)$ in (TMTSF)$_2$ClO$_4$, result in the odd and even Lebed magic angles, as observed experimentally [62, 79]. Our theory also explains why the Lebed oscillations are strong and the DKC oscillations are weak in (TMTSF)$_2$ReO$_4$, and vice versa in (TMTSF)$_2$ClO$_4$, as observed experimentally [61].

When a strong magnetic field is applied parallel to the layers, and B_y exceeds a certain threshold, then interlayer tunneling between different branches of the Fermi surface, produced by folding of the Brillouin zone, should become possible. This effect would be observed as a sharp increase of interlayer conductivity. It can be utilized for a direct measurement of the anion gap E_g. Theoretical description of this effect required a quantum-mechanical treatment of the wave functions confined to different layers and cannot be achieved within the framework of quasiclassical electron orbits on a warped Fermi surface.

Experimental observation of the high number of magic angles (up to 21 in Ref. [62]) demonstrates a very high level of quantum coherence achieved in the Q1D organic conductors at low temperatures. This is remarkable given that the $(\mathrm{TMTSF})_2\mathrm{X}$ materials have strong electron interactions. In different parts of their rich phase diagram, these materials have the Mott insulating phase and other exotic phases [1, 2]. It would be very interesting to study what happens to AMRO when the system is driven toward the Mott state using pressure or other variables.

We point out that the theory of the angular magnetoresistance oscillations (AMRO) in Q1D conductors is equivalent to the mathematically description of the Mach-Zehnder interference in a driven superconducting qubit [39, 40] and of laser cooling in ion traps [44]. Thus, the physics of Q1D conductors may have applications in quantum engineering well beyond the domain of solid-state material science.

2.7 Calculation of the matrix elements

In this Appendix, we calculate the matrix elements of interlayer tunneling introduced in Eq. (2.33).

In the case of $(\mathrm{TMTSF})_2\mathrm{ClO}_4$, the interlayer tunneling with the amplitude t_c occurs between the chains of the same type, as shown in Fig. 1.5(b) [72]. The in-plane Hamiltonians of two adjacent layers are given by the same expression

$$\hat{H} = \begin{pmatrix} E_g & 2t_b \cos(k_y b) \\ 2t_b \cos(k_y b) & -E_g \end{pmatrix}. \tag{2.40}$$

The eigenvalues $\lambda_\pm$ and the eigenvectors $|\psi_\pm\rangle$ of the Hamiltonian (2.40) are

$$\lambda_\pm = \pm\sqrt{[2t_b \cos(k_y b)]^2 + E_g^2}, \tag{2.41}$$

$$|\psi_\pm(k_y)\rangle = \frac{1}{N_\pm}\,(\lambda_\pm + E_g, 2t_b \cos k_y b), \tag{2.42}$$

$$N_\alpha = \sqrt{[2t_b \cos(k_y b)]^2 + (\lambda_\alpha + E_g)^2}. \tag{2.43}$$

The matrix elements of tunneling are proportional to the scalar products of the wave functions in adjacent layers:

$$M_{--} = \langle\psi_-(k_y + q_y)|\psi_-(k_y)\rangle, \tag{2.44}$$

$$M_{++} = \langle\psi_+(k_y + q_y)|\psi_+(k_y)\rangle \tag{2.45}$$

for tunneling between the same kinds of bands and

$$M_{-+} = \langle\psi_-(k_y + q_y)|\psi_+(k_y)\rangle \tag{2.46}$$

between different kinds of bands. It is clear from Eq. (2.46) that M_{-+} vanishes for $q_y = 0$ because $|\psi_+(k_y)\rangle$ and $|\psi_-(k_y)\rangle$ are orthogonal.

In the case of (TMTSF)$_2$ReO$_4$, the inter-layer tunneling with the amplitude t_c occurs between the chains of different types. The in-plane Hamiltonian of one layer has the form (2.40), whereas the sign of E_g is reversed in the Hamiltonian H' of another layer

$$H' = \begin{pmatrix} -E_g & 2t_b \cos(k_y b) \\ 2t_b \cos(k_y b) & E_g \end{pmatrix}. \tag{2.47}$$

The eigenvalues of H' are the same as in Eq. (2.41), but the corresponding eigenvectors are different

$$|\psi'_\pm(k_y)\rangle = \frac{1}{N'_\pm}(\lambda_\pm - E_g, 2t_b\cos k_y b), \tag{2.48}$$

$$N'_+ = N_-, \qquad N'_- = N_+. \tag{2.49}$$

The scalar products of the wave functions in the adjacent layers now are

$$M_{--} = \langle\psi'_-(k_y+q_y)|\psi_-(k_y)\rangle, \tag{2.50}$$

$$M_{++} = \langle\psi'_+(k_y+q_y)|\psi_+(k_y)\rangle \tag{2.51}$$

for the same kinds of bands and

$$M_{-+} = \langle\psi'_-(k_y+q_y)|\psi_+(k_y)\rangle \tag{2.52}$$

for different kinds of bands. Now M_{-+} does not vanish for $q_y = 0$, because $|\psi_+(k_y)\rangle$ and $|\psi'_-(k_y)\rangle$ are not orthogonal.

Chapter 3

Angular magnetoresistance oscillations in graphene bilayer

3.1 Introduction

Graphene is one atom-thick planar sheet of sp^2-bonded carbon atoms that are packed in a honeycomb crystal lattice which contains two inequivalent sublattices A and B (two atoms per unit 2D unit cell). It is the two-dimensional building block of carbon materials of every other dimensionality. It can be stacked into 3D graphite, rolled into 1D nanotubes, or 0D buckyballs. For decades scientists presumed that 2D graphite sheet could not exist in its free state; they reasoned that its planar structure would be thermodynamically unstable and possibly curl into carbon soot. However in 2005 groups in university of Manchester and Columbia university [82, 83] managed to isolate single graphene sheets and since then there has been a huge surge in graphene related research.

Even though the graphene sheet is an ideal realization of a two dimensional system, its properties differ markedly from the well-studied case of quantum wells in conventional semiconductor interfaces. Some unusual phenomena characteristic of graphene are the following: first, graphene's conductivity never falls below a minimum value corresponding to the quantum unit of conductance, even when concentration of charge carriers tend to zero [82]; second, the integer quantum Hall effect in graphene is anomalous in that it occurs at half integer filling factors [83];

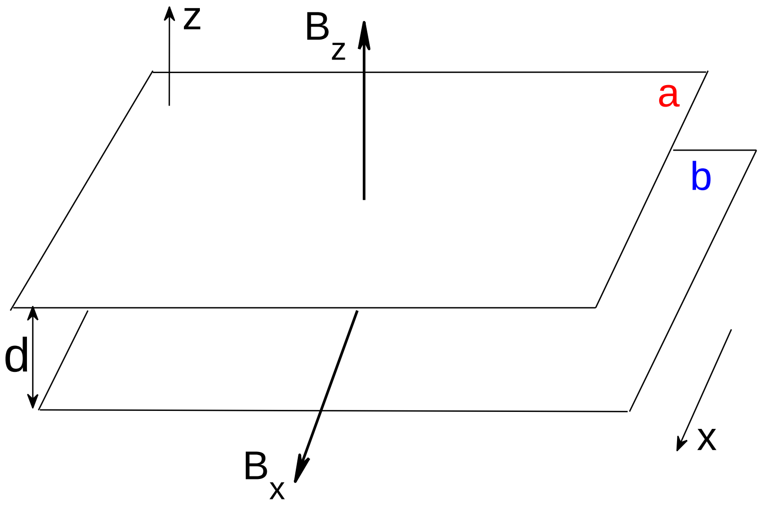

Figure 3.1: Figure shows the geometry of bilayer

and third, in graphene bilayers the plateaus in Hall conductivity occur at the standard integer positions, but the last (zero-level) plateau is missing [84]. In this chapter we study, how the unusual properties of graphene manifests itself in angular magnetoresistance oscillations (AMRO) in graphene bilayers.

The angular magnetoresistance oscillation were originally discovered in quasi-two-dimensional organic conductors of the (BEDT-TTF)$_2$X family [85, 86]. Upon rotation of magnetic field $\boldsymbol{B}$, electrical resistivity oscillates in $\tan\theta$, where θ is the angle between $\boldsymbol{B}$ and the normal to the layers. The oscillations are very strong and most pronounced in the interlayer resistivity ρ_z. AMRO are different from Shubnikov-de Haas (SdH) oscillations, where resistivity oscillates as a function of magnetic field for a fixed orientation. AMRO typically persists to substantially higher temperatures than SdH oscillations, so the two effects can be clearly separated experimentally. In the next section we give the details of the calculation of AMRO in metallic bilayers.

3.2 AMRO in metallic bilayers

Consider two independent metallic layers a and b separated by a distance d, as shown in Fig. 3.1. In a perpendicular magnetic field $\boldsymbol{B} = (0, 0, B_z)$ with the choice of vector potential $\boldsymbol{A} = (0, B_z x, 0)$, the Hamiltonian in the independent layers a and b is

$$\begin{aligned} H_{a,b} &= \frac{\hbar^2}{2m} k_x^2 + \frac{\hbar^2}{2m}(k_y - eB_z x)^2 \\ &= \frac{\hbar^2}{2m} k_x^2 + \frac{1}{2} m\omega_c^2 (x - l_\perp^2 k_y)^2 \end{aligned} \tag{3.1}$$

where $\omega_c = eB_z/m$ is the cyclotron frequency and $l_\perp = \sqrt{\hbar/eB_z}$ is the magnetic length. The eigenfunctions and the corresponding eigenvalues of $H_{a,b}$ are

$$\psi_n(x, y) = e^{ik_y y}\phi_n(x - l_\perp^2 k_y), \quad \epsilon_n = (n + 1/2)\hbar\omega_c \tag{3.2}$$

Here $\phi_n(x)$ is a one dimensional harmonic oscillator eigenfunction,

$$\phi_n(x) = (2^n n! \sqrt{\pi} x_0)^{-1/2} \exp\left[-\frac{1}{2}\left(\frac{x}{x_0}\right)^2\right] H_n\left(\frac{x}{x_0}\right), \quad x_0 = \sqrt{\frac{\hbar}{m\omega_c}} \tag{3.3}$$

H_n are the Hermite polynomials, and n is a non-negative integer representing the Landau level. When the possibility of hopping between the layers is included the two layers are coupled. The electron tunneling between the layers is described by the Hamiltonian

$$H_\perp = t_\perp \int \hat{\psi}_a^\dagger(\boldsymbol{r})\hat{\psi}_b(\boldsymbol{r}) e^{ieA_z(\boldsymbol{r})d/\hbar} d^2r + \text{H.c.} \tag{3.4}$$

$$A_z(\boldsymbol{r}) = B_x y \tag{3.5}$$

where $t_\perp$ is the interplane tunneling amplitude, e is the electron charge, $A_z(\boldsymbol{r})$ is the vector potential, $\hat{\psi}_{a,b}$ are the electron destruction operators in layers a and b and $\boldsymbol{r} = (x, y)$. We assume that the interlayer tunneling amplitude $t_\perp$ is small compared to the Fermi energy in each layer, so it can be treated as a perturbation. In the low-temperature limit the interlayer conductivity σ_{zz} is given by [87]

$$\sigma_{zz} = \sigma_0 \sum_{n,n'} \vartheta^2_{n,n'} \int\limits_{-\infty}^{\infty} [-f'(\zeta)] \rho_{a,n}(\zeta) \rho_{b,n'}(\zeta)\, d\zeta \tag{3.6}$$

where σ_0 is related to the conductivity at zero magnetic field (for the following calculations we set it equal to 1), f is the Fermi distribution function, ρ_n is density of states for the Landau level n and $\vartheta_{n,n'} = \langle \psi_{a,n} | H_\perp | \psi_{b,n'} \rangle / t_\perp$. In the low temperature limit we can approximate $-f'(\zeta) = \delta(\zeta - \mu)$, where μ is the chemical potential. Then taking only the diagonal contribution $n = n'$ in Eq. (3.6), we get

$$\sigma_{zz} = \sum_n \vartheta^2_{n,n}\, \rho^2_n(\mu) \tag{3.7}$$

We assume that in the low temperature limit the density of states are sharply peaked around the Landau levels and their spread is much smaller than $\hbar\omega_c$, the energy difference between the levels. Under this assumption, if the Fermi surface is between the Landau levels η and $\eta + 1$, then only the terms corresponding to these two levels will have a significant contribution to the interlayer conductivity. Thus, we can approximate the interlayer conductivity in Eq. (3.7) by

$$\sigma_{zz} = \sigma_0 \left[\vartheta^2_{\eta,\eta}\, \rho^2_\eta(\mu) + \vartheta^2_{\eta+1,\eta+1}\, \rho^2_{\eta+1}(\mu) \right] \tag{3.8}$$

Generally there is no accurate analytic expression for $\rho(\xi)$, we assume it has the form

$$\rho_n(\nu) = \exp\left(\frac{|\nu - n|^2}{\Gamma}\right), \tag{3.9}$$

where Γ is the damping of the levels and $\nu = \hbar k_F^2/2eB_z$ is a continuous index. The matrix element

$$\vartheta_{n,n} = \int_{-\infty}^{\infty} dx \int_{-\infty}^{\infty} dy\, \phi_n(x - l_\perp^2 k_y) e^{ieB_x yd/\hbar} \phi_n(x - l_\perp^2 k_y')\, e^{iy(k_y - k_y')}, \tag{3.10}$$

The integral can be evaluated analytically [88] and we obtain

$$\vartheta_{n,n} = e^{-w^2} L_n(2w^2), \quad w = \frac{B_x d}{2}\sqrt{\frac{e}{\hbar B_z}}, \tag{3.11}$$

where $L_n(\xi)$ are the Laguerre polynomials. Substituting Eq. (3.9) and (3.11) in Eq. (3.8), we get

$$\sigma_{zz} = \left[e^{-2p\alpha^2} L_p(4p\alpha^2)\right]^2 \exp\left[-\frac{(p-\nu)^2}{\Gamma}\right] + \left[e^{-2q\alpha^2} L_q(4q\alpha^2)\right]^2 \exp\left[-\frac{(\nu-q)^2}{\Gamma}\right] \tag{3.12}$$

where $\alpha = w\sqrt{2\nu} = edB_x/2\hbar k_F$, $p = \text{Int}(\nu)+1$ and $q = p - 1$. Fig. 3.2 shows the contour plot of σ_{zz} as a function of α and $1/\nu$ calculated from Eq. (3.12), for $\Gamma = 0.18$. The plot shows a rich pattern of oscillations. For a fixed orientation the of the magnetic field, the oscillations in the radial direction are the SdH oscillations and for a fixed magnitude of magnetic field the oscillations in the angular direction are the AMRO. All these oscillations can be interpreted as a particular manifestation of Aharanov-Bohm effect [75].

For $\nu \gg 1$ the ν-th Laguerre polynomial can be approximated by the Bessel

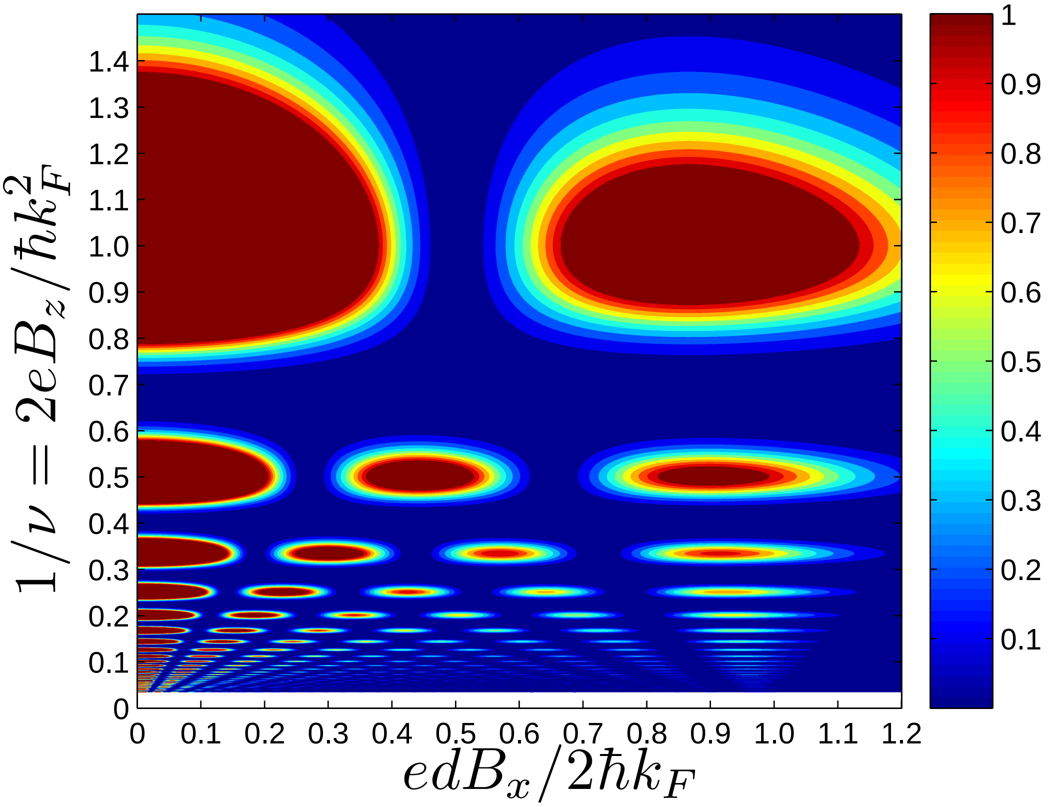

Figure 3.2: Contour plot of σ_{zz} in a metallic bilayer calculated from Eq. 3.12

.

function of order zero

$$L_\nu(\xi) \cong J_0\left(2\sqrt{\nu\xi}\right)\, e^{\xi/2}, \tag{3.13}$$

and the zero-th order Bessel function has the asymptotic form

$$J_0(\xi) \approx \sqrt{2/\pi\xi}\,\cos(\xi - \pi/4). \tag{3.14}$$

Using these approximations we get

$$\vartheta_{\nu,\nu} \approx \frac{\cos\left(4\nu\alpha - \pi/4\right)}{\sqrt{2\pi\nu\alpha}} = \sqrt{\frac{2}{\pi}}\frac{\cos\left(dk_F B_x/B_z - \pi/4\right)}{\sqrt{dk_F B_x/B_z}}. \tag{3.15}$$

From the above equation we see that the effective tunneling amplitude vanishes periodically with respect to $\tan\theta = B_x/B_z$. This gives rise to the peaks in resistivity in the z direction mentioned in the introduction.

3.3 Graphene energy levels in a perpendicular field

Electrical properties of graphene can be described by a conventional tight-binding model [89]. The tight-binding dispersion is

$$\varepsilon(\boldsymbol{k}) = \pm t\sqrt{1 + 4\cos^2 \pi k_y a + 4\cos \pi k_y a + 4\cos \pi k_y a\ \cos \pi k_x \sqrt{3}a} \tag{3.16}$$

where $t \approx 2.8$eV is the nearest-neighbor hopping amplitude, $a \approx 2.46$Åis the lattice constant, and $\boldsymbol{k} = (k_x, k_y)$ is the in plane wave vector. There are two bands, conduction band (corresponding to + sign) and valence band (corresponding to the - sign). The two bands touch each other at six different points in momentum space. However, only two (K and K') of these six points are independent, and the rest are equivalent by symmetry. The Hamiltonian at the vicinity of these one of these points (say K) has the form

$$H(\boldsymbol{p}) = v_F \begin{pmatrix} 0 & p_x + ip_y \\ p_x - ip_y & 0 \end{pmatrix} = v_F \begin{pmatrix} 0 & pe^{i\theta_p} \\ pe^{-i\theta_p} & 0 \end{pmatrix}, \quad \theta_p = \tan^{-1}(p_y/p_x) \tag{3.17}$$

where the Fermi velocity $v_F = 3at/2\hbar \approx 10^6$m/s. This Hamiltonian is well known in both condensed-matter and particle physics; in the latter case it is used to describe, e.g., a 2D massless neutrino. The eigenstates and the corresponding energies are given by [90, 91, 92]

$$|p\rangle = \frac{1}{\sqrt{2}} e^{i\boldsymbol{p}.\boldsymbol{r}/\hbar} \begin{pmatrix} b e^{i\theta_p/2} \\ e^{-i\theta_p/2} \end{pmatrix}, \quad E = b\hbar v_F p, \tag{3.18}$$

where $b = 1(-1)$ for the states above (below) the energy at K. Eq. (3.18) shows that the electron possesses a two-component vector that gives the amplitude of electronic wave function on the two sublattice atoms A and B. In a perpendicular magnetic field $\boldsymbol{B} = (0, 0, B_z)$ the Hamiltonian in the vicinity of the Dirac point K is

$$H(\boldsymbol{p}) = v_F \begin{pmatrix} 0 & p_x + i(p_y - eB_z x) \\ \text{c.c.} & 0 \end{pmatrix}, \tag{3.19}$$

The eigenvectors $\psi = \{\psi_A, \psi_B\}$ and corresponding eigenvalue ε satisfy the equation

$$v_F \begin{pmatrix} 0 & p_x \pm i(p_y - eB_z x) \\ \text{c.c.} & 0 \end{pmatrix} \begin{pmatrix} \psi_A \\ \psi_B \end{pmatrix} = \varepsilon \begin{pmatrix} \psi_A \\ \psi_B \end{pmatrix} \tag{3.20}$$

which simplifies to the operator equation

$$v_F^2 (p_\chi^2 + eB_z^2 \chi^2 - eB_z \hbar)\psi_A = \varepsilon^2 \psi_A \tag{3.21}$$

$$v_F^2 (p_\chi^2 + eB_z^2 \chi^2 + eB_z \hbar)\psi_B = \varepsilon^2 \psi_B, \tag{3.22}$$

where $\chi = x - l_\perp^2 k_y$. The above equations have the form of the Schrödinger equation for a one-dimensional harmonic oscillator. A comparison gives

$$\psi_K(\chi, y) = \begin{pmatrix} \phi_n(\chi) \\ \phi_{n-1}(\chi) \end{pmatrix} e^{ik_y y}, \quad \varepsilon_n = \pm\sqrt{2e\hbar v_F^2 n B_z} \tag{3.23}$$

where $n \geq 0$ represents the Landau level ($\phi_{-1}(\chi) = 0$). A similar calculation gives, in the vicinity of K'

$$\psi_{K'}(\chi, y) = \begin{pmatrix} \phi_{n-1}(\chi) \\ \phi_n(\chi) \end{pmatrix} e^{ik_y y}, \quad \varepsilon_n = \pm\sqrt{2e\hbar v_F^2 n B_z} \tag{3.24}$$

3.4 Interlayer conductivity in graphene bilayer

We assume that the interlayer tunneling amplitude between the graphene layers, $t_\perp$, is small compared with the interlayer energy scales, so it can be treated as a perturbation. First we consider the hexagonal stacking, shown in Fig. 3.3(a). In this case, all atoms in the lower layer are exactly below the atoms in the upper layer. Then the tunneling between the layers takes place from site A to A' and B to B'. Using Eq. (3.4) and (3.23) we get the matrix element

$$\vartheta_{n,n} = 2\int\limits_{-\infty}^{\infty} d\chi \int\limits_{-\infty}^{\infty} dy\, e^{ieB_x dy/\hbar}\Big[\phi_n(\chi)\phi_n(\chi+s)+\phi_{n-1}(\chi)\phi_{n-1}(\chi+s)\Big]e^{ik_y y}e^{-ik'_y y}, \tag{3.25}$$

where $s = \hbar(k_y - k'_y)/eB_z$. Integrating the above equation with respect to y gives

$$\vartheta_{n,n} = 4\pi\int\limits_{-\infty}^{\infty} d\chi\, \left[\phi_n(\chi)\phi_n(\chi+s)+\phi_{n-1}(\chi)\phi_{n-1}(\chi+s)\right]\delta\left(k_y - k'_y + \frac{eB_x d}{\hbar}\right) \tag{3.26}$$

k_y is a good quantum number and therefore during tunneling the electron momentum in y direction is conserved. From the δ function we get the momentum conservation equation $k_y = k'_y + eB_x d/\hbar$. Substituting this in the above equation we get

$$\vartheta_{n,n} = 4\pi\int\limits_{-\infty}^{\infty} d\chi\, \left[\phi_n\left(\chi+\frac{B_x d}{2B_z}\right)\phi_{n'}\left(\chi-\frac{B_x d}{2B_z}\right)+\phi_{n-1}\left(\chi+\frac{B_x d}{2B_z}\right)\phi_{n'-1}\left(\chi-\frac{B_x d}{2B_z}\right)\right]. \tag{3.27}$$

These integrals can be evaluated analytically to get (ignoring the multiplicative constants)

$$\vartheta_{n,n} = e^{-w^2}\Big[L_n(2w^2)+L_{n-1}(2w^2)\Big] = e^{-2n\alpha^2}\Big[L_n(4n\alpha^2)+L_{n-1}(4n\alpha^2)\Big], \tag{3.28}$$

where $L_n(\xi)$ are the Laguerre polynomials. There are two terms corresponding to tunneling between different kind of sites. The interlayer conductivity is square to tunneling amplitude and therefore depends on the interference of these two terms. Substituting Eq. 3.28 in Eq. 3.8 we get

$$\begin{aligned}\sigma_{zz} &= \left[e^{-2p\alpha^2}\left(L_p(4p\alpha^2) + L_{p-1}(4p\alpha^2)\right)\right]^2 \exp\left[-\frac{(p-\nu)^2}{\Gamma}\right] + \\ &\left[e^{-2q\alpha^2}\left(L_q(4n\alpha^2) + L_{q-1}(4q\alpha^2)\right)\right]^2 \exp\left[-\frac{(\nu-q)^2}{\Gamma}\right] \qquad (3.29)\end{aligned}$$

Fig. 3.4 shows the contour plot of σ_{zz} as a function of α and $1/\nu$, calculated using Eq. (3.29), for $\Gamma = 0.18$. For small parallel field the interlayer conductivity shows oscillation patterns similar to metallic bilayer but at large field the oscillations are suppressed. This is because at large parallel fields, the tunneling takes place from state $|p(\theta = 0)\rangle$ in one layer to $|p(\theta = \pi)\rangle$ in the other layer. Using Eq. 3.18 we see that $\langle p(\theta = \pi)|p(\theta = 0)\rangle = 0$, hence the tunneling is suppressed.

Next we consider the case where the graphene layers are shifted relative to each other, as shown in Fig. 3.3. This structure is known as the Bernal structure [93]. In this case the interlayer tunneling takes place between sites A and B' and there is no tunneling from A' and B. Thus, tunneling takes place between half of the atoms in each layer. Using Eq. (3.4)and (3.23) we get the effective interlayer tunneling amplitude

$$\vartheta_{n,n} = \int_{-\infty}^{\infty} d\chi \int_{-\infty}^{\infty} dy\, e^{ieB_x dy/\hbar} \left[\phi_n(\chi)\phi_{n-1}(\chi + s) + \phi_{n-1}(\chi)\phi_n(\chi + s)\right] e^{ik_y y} e^{-ik'_y y} \qquad (3.30)$$

Integrating the above equation with respect to y gives

$$\vartheta_{n,n} = 2\pi \int_{-\infty}^{\infty} d\chi \left[\phi_n(\chi)\phi_{n-1}(\chi+s) + \phi_{n-1}(\chi)\phi_n(\chi+s) \right] \delta\left(k_y - k_y' + \frac{eB_x d}{\hbar} \right) \quad (3.31)$$

Conservation of momentum in y-direction gives $k_y = k_y' + edB_x/\hbar$, substituting this in the previous equation we get

$$\vartheta_{n,n} = 2\pi \int_{-\infty}^{\infty} d\chi \left[\phi_n\left(\chi + \frac{B_x d}{2B_z}\right) \phi_{n-1}\left(\chi - \frac{B_x d}{2B_z}\right) + \phi_{n-1}\left(\chi + \frac{B_x d}{2B_z}\right) \phi_n\left(\chi - \frac{B_x d}{2B_z}\right) \right]. \quad (3.32)$$

The two integrals are equal and can be evaluated analytically to get

$$\vartheta_{n,n} = 4\pi\sqrt{\frac{2}{n}} w e^{-w^2} L^1_{n-1}(2w^2) = 8\pi\alpha e^{-2n\alpha^2} L^1_{n-1}(4n\alpha^2), \quad (3.33)$$

where $L^1_n(\xi)$ is the generalized Laguerre polynomial. In this case the effective tunneling amplitude contains only one term because there is only one kind of tunneling (A to B'). Substituting the above into Eq. (3.8) equation get

$$\sigma_{zz} = \left[\alpha e^{-2p\alpha^2} L^1_{p-1}(4p\alpha^2)\right]^2 \exp\left[-\frac{(p-\nu)^2}{\Gamma}\right] + \left[\alpha e^{-2q\alpha^2} L^1_{q-1}(4q\alpha^2)\right]^2 \exp\left[-\frac{(\nu-q)^2}{\Gamma}\right] \quad (3.34)$$

Fig. 3.5 shows the contour plot of σ_{zz} as a function of α and $1/\nu$ calculated from Eq. (3.34), for $\Gamma = 0.18$. The oscillation patterns are significantly different from the hexagonal stacking case. For zero parallel field the conductivity is suppressed because the wavefunctions at the sites A and B' are like spinors of the form $\{\phi_n, \phi_{n-1}\}$ and $\{\phi_{n'-1}, \phi_n\}$. These wave functions are orthogonal to each other, and therefore there cannot be any tunneling between them.

3.5 Dispersion in parallel field

In this section we discuss the effects of a parallel magnetic field on the low energy band structure of graphene bilayers. In graphene a bilayer, the interlayer tunneling amplitude $t_\perp \approx 300$meV. Here we consider the case where the intralayer energy scales are smaller than $t_\perp$. Thus, we cannot treat $t_\perp$ as a perturbation, and an exact treatment is required. In this section we consider only the Bernal structure, shown in Fig. 3.3. The interlayer tunneling takes place between the sites A and B' only. Using the model of graphene bilayer described in Ref. [94], the Hamiltonian in the vicinity of one of the Dirac points (say K) is

$$H(\boldsymbol{p}) = v_F \begin{pmatrix} \Delta & pe^{i\phi(\boldsymbol{p})} & t_\perp/v_F & 0 \\ pe^{-i\phi(\boldsymbol{p})} & \Delta & 0 & 0 \\ t_\perp/v_F & 0 & -\Delta & pe^{-i\phi(\boldsymbol{p})} \\ 0 & 0 & pe^{i\phi(\boldsymbol{p})} & -\Delta \end{pmatrix}, \tag{3.35}$$

where $\boldsymbol{p} = (p_x, p_y)$ is the in-plane momentum measured from the K, $\phi(\boldsymbol{p}) = \tan^{-1}(p_y/p_x)$ and Δ is a measure of the asymmetry between the layers. Fig. 3.6 shows the plot of the energy bands calculated from Eq. 3.35, for symmetric layers ($\Delta = 0$). The coupling between the two graphene layers transforms the massless Dirac fermions, characteristic of single-layer graphene, into a new type of quasiparticles which have an ordinary parabolic spectrum $\varepsilon(p) = p^2/2m$. Now, if we introduce a parallel magnetic field $\boldsymbol{B} = (0, B_y, 0)$, then with the choice of the vector potential

$\boldsymbol{A} = (-B_y z, 0, 0)$, the Hamiltonian in Eq. 3.35 becomes

$$H(\boldsymbol{p}) = v_F \begin{pmatrix} \Delta & (p_x + q/2) + ip_y & t_\perp/v_F & 0 \\ (p_x + q/2) - ip_y & \Delta & 0 & 0 \\ t_\perp/v_F & 0 & -\Delta & (p_x - q/2) - ip_y \\ 0 & 0 & (p_x - q/2) + ip_y & -\Delta \end{pmatrix}, \tag{3.36}$$

where $q = ezB_y$ and e is the charge of an electron. Here z is a good quantum number representing the vertical position of the two layers. We assume that the two layers are at $z = \pm d/2$, where $d \approx 0.34$nm is the experimentally measured separation between the layers in graphene bilayer. Fig. 3.7(a) shows the plot of the energy bands as a function of (p_x, p_y), calculated from the Hamiltonian in Eq. (3.36). The qualitative features of the band structure can be understood in terms of the band structure of graphene. As the electrons tunnel from one layer to another, due to the magnetic field in the y direction, they feel an impulse in the x direction (due to Lorentz force). The impulse causes a momentum shift between the energy bands of the two layers, and the two Dirac cones are shifted relative to each other by momentum q. Due to the momentum shift the Dirac points do not overlap. As the two cones hybridize due to interlayer coupling, the two Dirac points are preserved and reappear at $p_x = \pm q/2$. The analytical form of the energy bands are

$$\lambda_1(p_x) = \frac{v_F}{2}\sqrt{q^2 + 2\gamma^2 + 4p_x^2 - 2\sqrt{q^2\gamma^2 + \gamma^4 + 4q^2p_x^2 + 4p_x^2\gamma^2}}, \quad \lambda_2(p_x) = -\lambda_1(p_x). \tag{3.37}$$

where $\gamma = t_\perp / v_F$. Fig. 3.7(b) shows the plot of these two bands as a function of p_x. Expanding the function $\lambda_1(p_x)$ around $p_x = q/2$ we obtain

$$\lambda_1(p_x) = \frac{q v_F}{\sqrt{q^2 + \gamma^2}} (p_x - q/2) \tag{3.38}$$

As expected, close to $p_x = \pm q/2$, energy depends linearly on momentum. This implies that the Dirac-like spectrum, which was lost in graphene bilayers due to the interlayer coupling, can be recovered by applying a parallel magnetic field between the layers. As mentioned earlier the Quantum Hall effect in graphene-bilayer and graphene are different. With a parallel magnetic field, at low energies, we can tune between a graphene bilayer dispersion and a graphene-like dispersion (two Dirac-like cones in Fig. 3.7). This opens up an interesting question: can there be a continuous Quantum Hall effect ?

Generically the two layers in a graphene bilayer would always be asymmetric ($\Delta = 0$ is an ideal case); therefore in general $\Delta \neq 0$. Fig. 3.8 shows the energy bands calculated from Eq. 3.35 for $\Delta \neq 0$. Notice that a gap opens up between the valance and the conduction band. This gap can be tuned by changing Δ by doping the layers or by applying a gate bias. This gap has great importance as it makes graphene bilayer the only known semiconductor with a tunable energy gap and opens up the possibility of developing tunable photo detectors and lasers. If a parallel magnetic field is applied, then the low energy bands get further modified. Fig. (3.9) shows the two low energy bands calculated for different values of q/Δ. Thus along with Δ, the parallel magnetic fields become a second parameter by which the low energy bands of graphene bilayer can be modified.

For all plot we chose the parameters q, Δ and $t_\perp$ to have comparable values. For large magnetic field, like $B_y = 50T$, $v_F q = v_F e d B_y$ =17mev. This means that $v_F q/t_\perp \sim 1/15$. This is much smaller than the values that we used in our plots. Thus, the effects that we mentioned above might be a little too small to measure in an experiment.

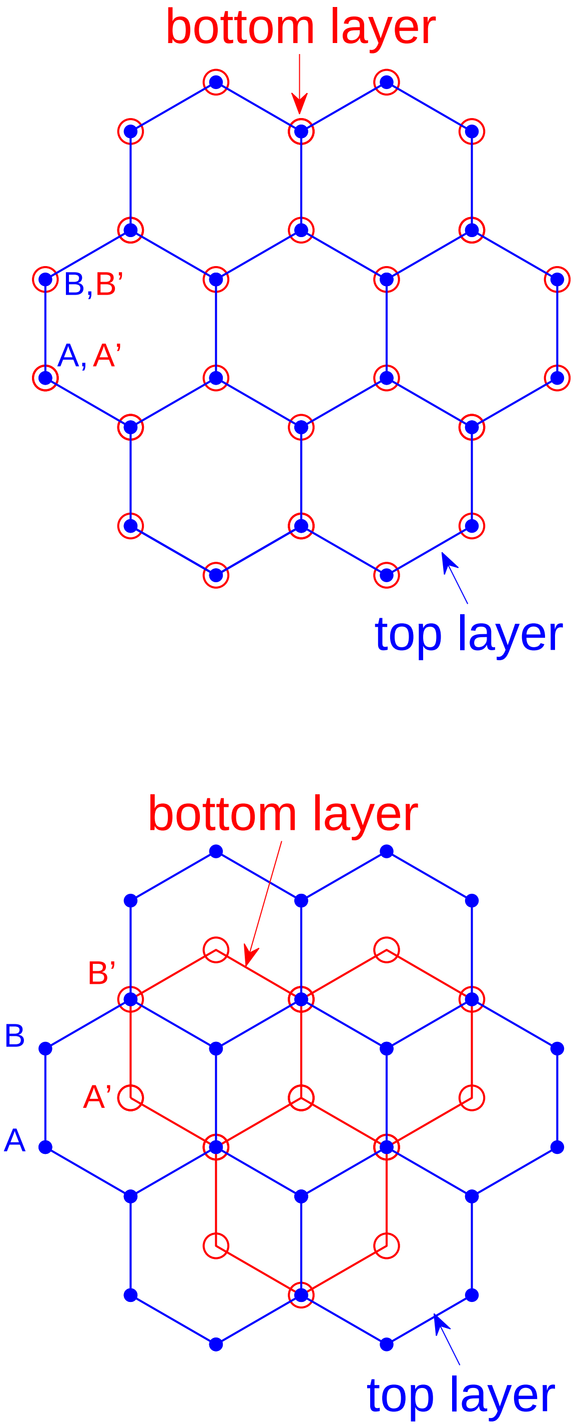

Figure 3.3: Top view of the arrangement of the carbon atoms in graphene layers in (a) Hexagonal stacking (b) Bernal stacking

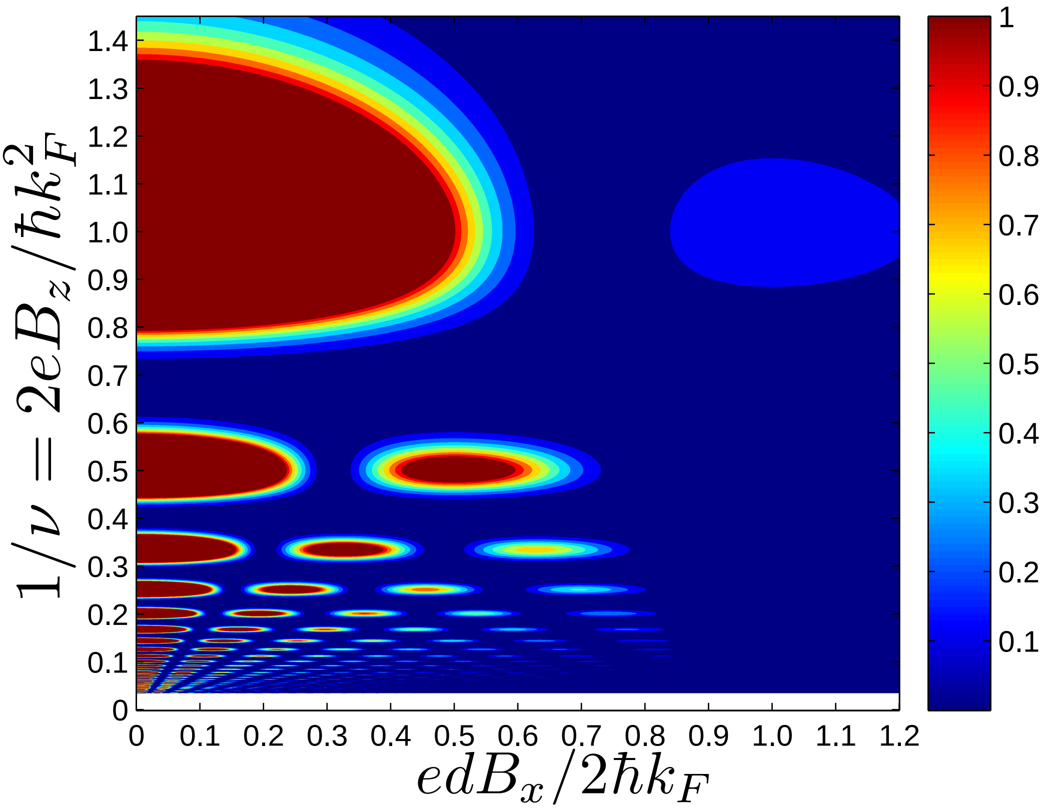

Figure 3.4: Contour plot of σ_{zz} in graphene bilayer, calculated from Eq. 3.29. The layers are stacked according to hexagonal stacking

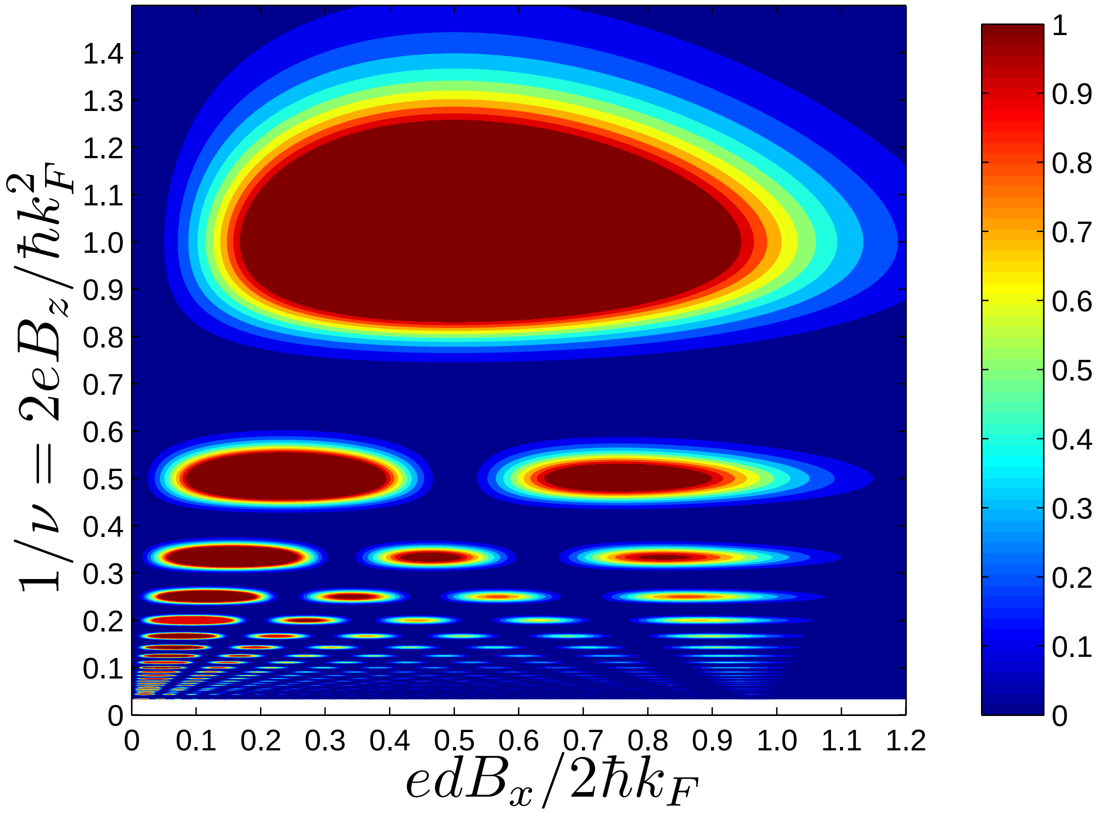

Figure 3.5: Contour plot of σ_{zz} in graphene bilayer, calculated from Eq. 3.34. The layers are stacked according to Bernal stacking

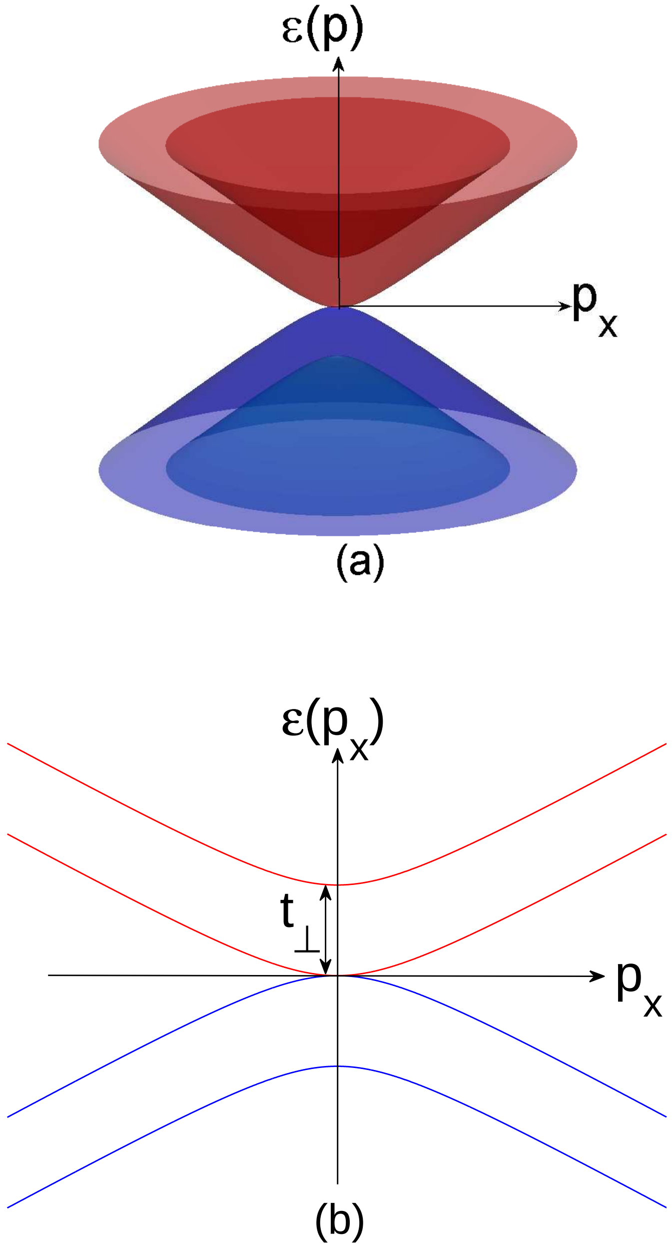

Figure 3.6: Plot shows the band structure of graphene bilayer for $\Delta = 0$. (a) Shows the band structure as a function of (p_x, p_y), (b) shows the vertical section of the plot in (a) for $p_y = 0$.

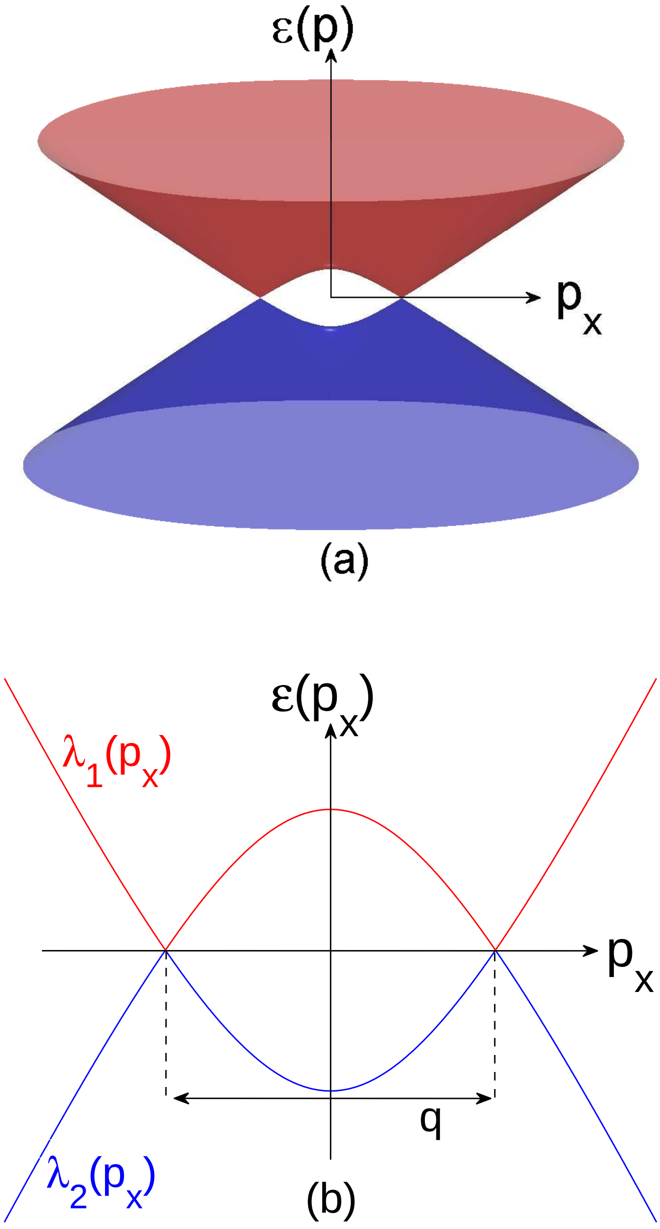

Figure 3.7: (a) Plot of the low energy bands of graphene bilayer in a parallel magnetic field, (b) Vertical section of the plot in (a). In a parallel magnetic field Dirac like cones reappear.

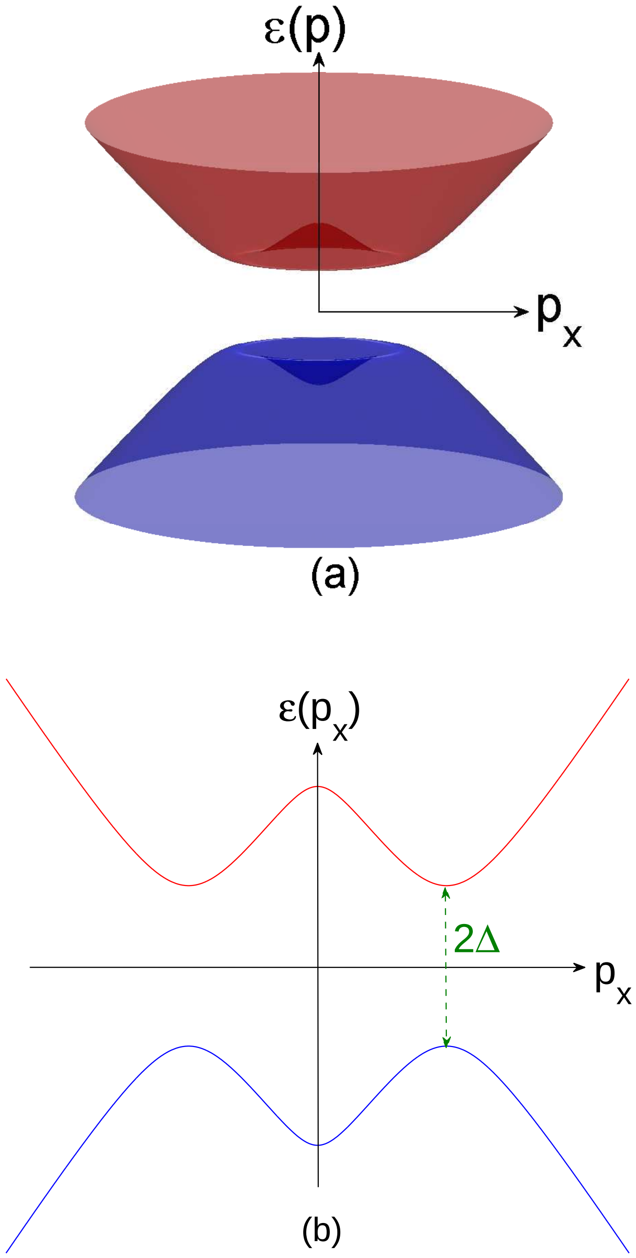

Figure 3.8: Plot of the energy bands of graphene bilayer for asymmetric layers ($\Delta \neq 0$). Energy gap of the order of Δ open up between the two low energy bands

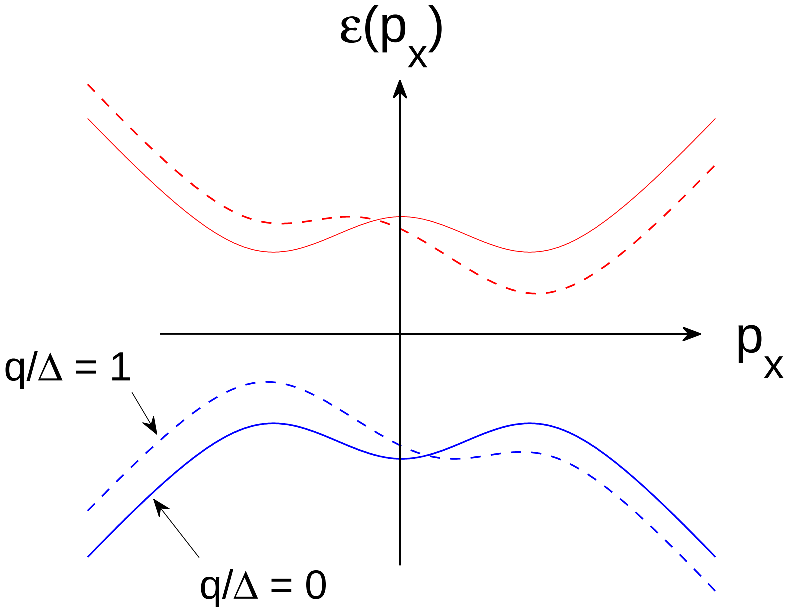

Figure 3.9: Plot of the low energy band in graphene bilayer. The $q/\Delta = 1$ curve shows that the bands can be modified by applying a parallel magnetic field

Chapter 4

A study of the personal income distribution in Australia

Distribution of income x is characterized by the probability density function (PDF) $P(x)$, defined so that the probability to find income in the interval from x to $x+dx$ is equal to $P(x)\,dx$. The PDFs for the distributions discussed above have the following functional forms:

$$P(x) \;=\; \begin{cases} \frac{1}{T}\exp(-x/T) & \text{exponential,} \\ \frac{1}{xs\sqrt{2\pi}}\exp\left[\frac{-\log^2(x/m)}{2s^2}\right] & \text{log-normal,} \\ \frac{(\beta)^{-(1+\alpha)}}{\Gamma(1+\alpha,0)}x^{\alpha}\exp(-x/\beta) & \text{gamma.} \end{cases} \tag{4.1}$$

The exponential distribution has one parameter T, and its $P(x)$ is maximal at $x = 0$. The log-normal and gamma distributions have two parameters each: (m, s) and (β, α). They have maxima (called modes in mathematical statistics) at $x = m\exp^{-s^2}$ and $x = \alpha\beta$, and their $P(x)$ vanish at $x = 0$. Many researchers impose the condition $P(0) = 0$ *a priori*, "because people cannot live on zero income". However, this assumption must be checked against the real data.

In this chapter, we analyze statistical data on personal income distribution in Australia for 1989–2000 and compare them with the three functions in Eq. (4.1). The data were collected by the Australian Bureau of Statistics (ABS) using surveys of population. The anonymous data sets give annual incomes of about 14,000 representative individuals, and each individual is assigned a weight. The weights add up to 1.3×10^7 to 1.5×10^7 in the considered period, which is comparable to the current population of Australia of about 20 million people. In the data analysis, we exclude individuals with negative and zero income, whose total weight is about 7%. These ABS data were studied in the previous paper [48], but without weights and with the emphasis on the Pareto tail at high income. Here we re-analyze the data in the middle and low income range covering about 99% of the population, but excluding the Pareto tail. The number of data points in the Pareto tail is relatively small in surveys of population, which complicates accurate analysis of the tail.

4.1 Cumulative Distribution Function

In this Section, we study the cumulative distribution function (CDF) $C(x) = \int_x^\infty P(x')\,dx'$. We sort incomes x_n of N individuals in decreasing order, so that $n = 1$ corresponds to the highest income, $n = 2$ to the second highest, etc. When the individuals are assigned the weights w_n, the cumulative probability for a given x_n is $C = \sum_{k=1}^{n} w_k / \sum_{k=1}^{N} w_k$, i.e. $C(x)$ is equal to the normalized sum of the weights of the individuals with incomes above x. We fit the empirically constructed $C(x)$ to the theoretical CDFs corresponding to Eq. (4.1)

$$C(x) = \begin{cases} \exp(-x/T) & \text{exponential,} \\ \frac{1}{2}\left[1 - \mathrm{Erf}\left(\frac{\log(x/m)}{s\sqrt{2}}\right)\right] & \text{log-normal,} \\ \Gamma(1+\alpha, x/\beta)/\Gamma(1+\alpha, 0) & \text{gamma,} \end{cases} \tag{4.2}$$

where $\mathrm{Erf}(x) = \frac{2}{\sqrt{\pi}} \int_0^x e^{-z^2}\,dz$ is the error function, and $\Gamma(\alpha, x) = \int_x^\infty z^{\alpha-1} e^{-z}\,dz$.

To visualize $C(x)$, different scales can be used. Fig. 4.1(a) uses the log-linear scale, i.e. shows the plot of $\ln C$ vs. x. The main panel in Fig. 4.1(b) uses the linear-

linear scale, and the inset the log-log scale, i.e. $\ln C$ vs. $\ln x$. We observe that the log-linear scale is the most informative, because the data points approximately fall on a straight line for two orders of magnitudes, which suggests the exponential distribution. To obtain the best fit in the log-linear scale, we minimize the relative mean square deviation $\sigma^2 = \frac{1}{M}\sum_{i=1}^{M}\left(\frac{C_e(x_i)-C_t(x_i)}{C_e(x_i)}\right)^2 \approx \frac{1}{M}\sum_{i=1}^{M}\{\ln[C_e(x_i)] - \ln[C_t(x_i)]\}^2$ between the empirical $C_e(x)$ and theoretical $C_t(x)$ CDFs. For this sum, we select $M = 200$ income values x_i uniformly spaced between $x = 0$ and the income at which CDF is equal to 1%, i.e. we fit the distribution for 99% of the population. The minimization procedure was implemented numerically in Matlab using the standard routines.

For the exponential distribution, the fitting parameter T determines the slope of $\ln C$ vs. x and has the dimensionality of Australian dollars per year, denoted as AUD or simply \$ (notice that $1\,\text{k\$} = 10^3\,\$$). T is also equal to the average income $\langle x\rangle$ for the exponential distribution. The parameters m and β for the log-normal and gamma distributions also have the dimensionality of AUD, and the average incomes $\langle x\rangle$ for these two distributions are $me^{s^2/2}$ and $\beta\Gamma(\alpha+2,0)/\Gamma(\alpha+1,0)$. The parameters s and α are dimensionless and characterize the shape of the distributions. The values of these parameters, obtained by fits for each year, are given in Table 4.1. Using the values of T, we plot C vs. x/T in Fig. 4.1. In these coordinates, the CDFs for different years (shown by different symbols) collapse on a single curve for the lower 98% of the population. The collapse implies that the shape of income distribution is very stable in time, and only the scale parameter T changes in nominal dollars. The three lines in Fig. 4.1 show the plots of the theoretical CDFs given by Eq. (4.2). In these coordinates, the exponential CDF is simply a straight line with the slope -1. For the plots of the log-normal and gamma CDFs, we used the parameters $\overline{s} = 0.72$, $\overline{m/T} = 0.88$, $\overline{\alpha} = 0.38$, and $\overline{\beta/T} = 0.77$ obtained by averaging of the parameters in Table 4.1 over the years. We observe that all three theoretical functions give reasonably good, albeit not perfect, fits of the data with about the same quality, as confirmed by the values of σ in Table 4.1. Although the log-normal and gamma distributions have the extra parameters s and α, the fitting procedure selects their values in such a way that these distributions mimic the exponential shape. Actually, we constructed the gamma fit only for 98% of the population, because the fit for 99% gives $\alpha = 0$, i.e. the exponential. We conclude that the exponential distribution gives a reasonable fit of the empirical CDFs with only one fitting parameter, whereas the log-normal and gamma distributions with more fitting parameters do not improve the fit significantly and simply mimic the exponential shape.

However, by construction, $C(x)$ is always a monotonous function, so one may argue that different CDFs look visually similar and hard to distinguish. Thus, it is instructive to consider PDF as well, which we do in the next Section.

4.2 Probability Density Function

In order to construct $P(x)$, we divide the income axis into bins of the width Δx, calculate the sum of the weights w_n of the individuals with incomes from x to $x+\Delta x$, and plot the obtained histogram. However, there is subjectiveness in the choice of the width Δx of the bins. If the bins are too wide, the number of individuals in each bin is big, so the statistics is good, but fine details of the PDF are lost. If the bins are too narrow, the number of individuals in each bin is small, thus relative fluctuations are big, so the histogram of PDF becomes noisy. Effectively, $P(x)$ is a derivative of the empirical $C(x)$. However, numerical differentiation increases noise and magnifies minor irregularities of $C(x)$, which are not necessarily important when we are interested in the universal features of income distribution. To illustrate these problems, we show PDFs obtained with two different bin widths in Fig. 4.2.

Fig. 4.2(a) shows the coarse-grained histogram of $P(x)$ for all years with a wide bin width $\Delta x/T \approx 0.43$. The horizontal axis represents income x rescaled with the values of T from Table 4.1. The lines show the exponential, log-normal, and gamma fits with the same parameters as in Fig. 4.1. With this choice of the bin width, the empirical $P(x)$ is a monotonous function of x with the maximum at $x = 0$, and the exponential function gives a reasonable overall fit. The log-normal and gamma fits have maxima at $x/T \approx 0.56$ and $x/T \approx 0.29$. These values are close to the bin width, so we cannot resolve whether $P(x)$ has a maximum at $x = 0$ or at a non-zero x within the first bin.

Fig. 4.2(b) shows the PDF for the year 1994-95 with a narrow bin width $\Delta x = 1$ k\$, which corresponds to $\Delta x/T \approx 0.05$. This PDF cannot be fitted by any of the three distributions, because it has a very sharp and narrow peak at the low income 7.3 k\$, which is way below the average income of 19.6 k\$ for this year. This peak is present for all years, and its position is reported in the last column of Table 4.1. The peak is so sharp and narrow that it cannot be attributed to the broad maxima of the log-normal or gamma PDFs. We speculate that this peak occurs at the threshold income of some sort of government policy, such as social welfare, minimal wage, or tax exemption. Comparing the empirical PDF with the exponential curve, shown by the solid line, we infer that the probability density above and below the peak is transferred to the peak, thus creating anomalously high population at the special income.

We also studied how often different income values occur in the data sets. The most frequently reported incomes for different years are always round numbers, such as 15 k\$, 20 k\$, 25 k\$, etc. This effect can be seen in the periodically spaced spikes in Fig. 4.2(b). It reflects either the design of the survey questionnaires, or the habit of people for rounding their incomes in reporting. In addition to the round numbers, we also find the income corresponding to the peak position among the five most frequently reported incomes. This income, shown in the last column in Table 4.1, is not round and changes from year to year, but sometimes stays the same. This again suggests that the sharp peak in Fig. 4.2(b) is the result of a government-imposed policy and cannot be explained by statistical physics arguments.

By definition, $P(x)$ is the slope of $C(x)$ with the opposite sign. Fig. 4.1 clearly shows that the slope of $C(x)$ at $x = 0$ is not zero, so $P(x = 0) \neq 0$. Fig. 4.2(b) also shows that the probability density at zero income is not zero. In fact, $P(x = 0)$ is higher than $P(x)$ for all other x, except in the narrow peak. The non-vanishing $P(x = 0)$ is a strong evidence against the log-normal, gamma, and similar distributions, but is qualitatively consistent with the exponential function. However, there is also substantial population with zero and negative income, which is not described by any of these theories.

4.3 Discussion and Conclusions

All three functions in Eq. (4.1) are the limiting cases of the generalized beta distribution of the second kind (GB2), which is also discussed in econometric literature on income distribution [95]. GB2 has four fitting parameters, and distributions with even more fitting parameters are considered in literature [95]. Generally, functions with more parameters are expected fit the data better. However, we do not think that increasing the number of free parameters gives a better insight into the problem. We think that a useful description of the data is the one that has the minimal number of parameters, yet reasonably (but not necessarily perfectly) agrees with the data. From this point of view, the exponential function has the advantage of having only one parameter T over the log-normal, gamma, and other distributions with more parameters. Fig. 4.1(a) shows that $\log C$ vs. x is approximately a straight line for about 98% of population, although small systematic deviations do exist. The log-normal and gamma distributions do not improve the fit significantly, despite having more parameters, and actually mimic the exponential function. Thus we conclude that the exponential function is the best choice.

The analysis of PDF shows that the probability density at zero income is clearly not zero, which contradicts the log-normal and gamma distributions, but is consistent with the exponential one, although the value of $P(x = 0)$ is somewhat lower than expected. The coarse-grained $P(x)$ is monotonic and consistent with the exponential distribution. The high resolution PDF shows a very sharp and narrow peak at low incomes, which, we believe, results from redistribution of probability density near the income threshold of a government policy. Technically, none of the three function in Eq. (4.1) can fit the complicated, three-peak PDF shown in Fig. 4.2. However, statistical physics approaches are intended to capture only the baseline of the distribution, not its fine features. Moreover, the deviation of the actual PDF from the theoretical exponential curve can be taken as a measure of the impact of government policies on income redistribution.

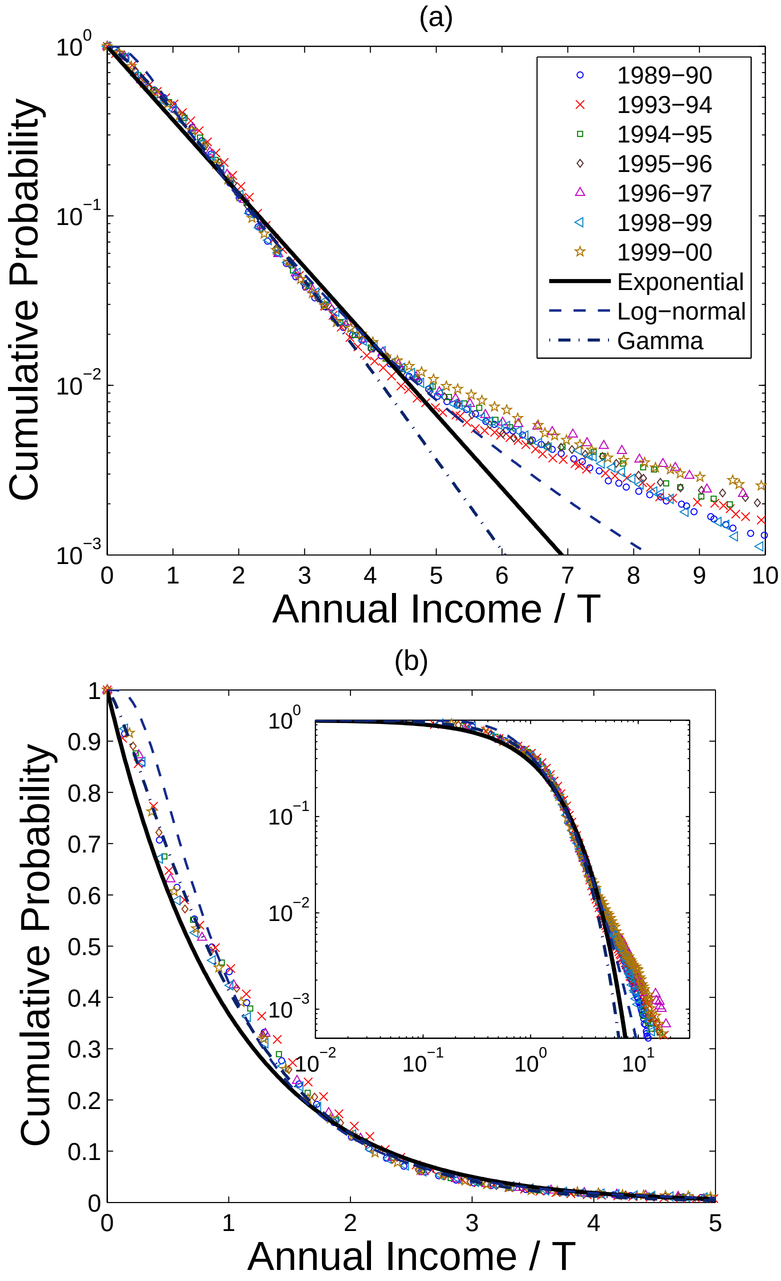

Figure 4.1: The cumulative distribution function (CDF) of income, shown in the log-linear (a), linear-linear (b), and log-log (inset) scales. The income values for different years are normalized to the parameter T of the exponential distribution, given in Table 4.1. The lines show fits to different theoretical distributions in Eq. (4.2).

Table 4.1: Parameters of the distributions (4.1) and (4.2) obtained by minimization of the relative mean square deviation σ^2 between the empirical and theoretical CDFs. The last column gives position of the sharp peak in Fig. 4.2(b).

Year	T	m	s	β	α	σ			Peak
	k$	k$		k$		Exp	L-N	Gamma	$
1989-90	17.8	15.1	0.74	13.4	0.39	13%	11%	6.8%	6196
1993-94	18.5	18.8	0.63	13.1	0.59	18%	9.6%	5.7%	7020
1994-95	19.6	17.7	0.71	14.9	0.40	15%	9.4%	5.5%	7280
1995-96	20.5	18.2	0.72	15.7	0.39	14%	8.6%	6.5%	7280
1996-97	21.2	18.9	0.72	16.5	0.37	14%	8.4%	7.7%	7540
1998-99	23.7	19.0	0.79	19.6	0.25	10%	11%	7.1%	7800
1999-00	24.2	19.6	0.78	19.3	0.30	11%	11%	7.2%	7800

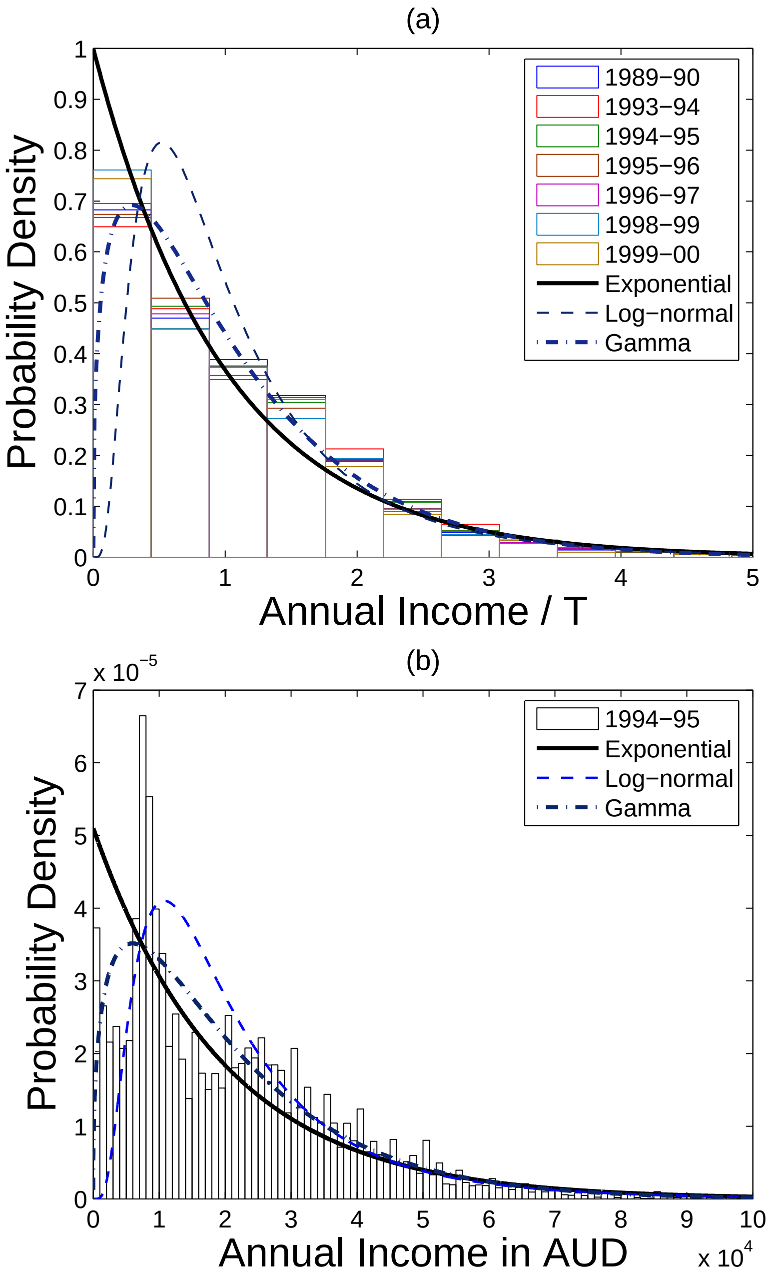

Figure 4.2: The probability density function (PDF) of income distribution shown with coarse-grained (a) and high (b) resolutions. The lines show fits to different theoretical functions in Eq. (4.1).

Chapter 5

Individual Income Distribution: Modeling and Empirical Study

In Ref. [55] Silva and Yakovenko studied the temporal evolution of income distribution in the USA for the years 1983-2001. They found that the personal income distribution has a well-defined two-class structure. The majority of population $(97-99\%)$ belongs to the lower class characterized by the exponential Boltzmann-Gibbs distribution, whereas the upper class $(1-3\%$ of the population) has a Pareto power law distribution. In section 5.1 we extend that study to subsequent years 2002-2006 (presently the latest year available).

Modeling of individual income distribution has a long history. A reasonable approach which is quite popular in economic literature [46, 47, 96], is to model income dynamics as a stochastic process and study its corresponding stationary solution. In section 5.2 we describe a model in which the income dynamics is treated as a sum of additive and multiplicative stochastic processes. The model captures the two-class structure of individual income distribution found in Ref. [55].

In section 5.3 we analyze data from an unusual source, University of Maryland's (UMD) campus newspaper "The Diamondback". Maryland state law requires the salaries of state employees be made public and thus each year "The Diamondback" publishes an extensive, annual database of salaries of university employees [97]. The employees contain professors, administrators, coaches, housekeepers, health center employees and dining hall workers. The data contains annual income of a large number of employees over a fairly broad range of income. We investigate the question that whether this data is a good representation of the overall trend of income distribution in the USA.

5.1 Internal Revenue Service data

We follow the notation used in chapter 4, $P(r)\,dr$ is the probability to find income in the interval from r to $r + dr$ and the cumulative distribution function $C(r) = \int_r^\infty P(r')\,dr'$. The publicly available data from IRS is preprocessed into income bins. This effectively gives the cumulative distribution function $C(r)$ for certain values of r. First we made plots of $C(r)$ vs. r for each year, in log-linear scale. We found the plots are straight lines for the lower 94-97% of the population. Straight lines in log-linear scale suggests that this part of the population follows the exponential distribution. By fitting $C(r)$ with the function $\exp(-r/T)$, we found the average income T for each year. Fig. 5.1 shows the plot of $C(r)$ vs. r/T in log-linear scale. The columns of numbers list the values of the average income T for the corresponding year. In these coordinates the data points for different years collapse onto a straight line, which shows that this part of the distribution is very stable in time and does not change at all over the years.

Fig. 5.2 shows the plot of $C(r)$ vs. r/T in log-log scale for a wider range of income r. The data points at low income are the same as the ones shown in Fig. 5.1. As expected, the data points for different years collapse onto a single exponential curve for the lower part of the distribution. However above a certain income $r_* \approx 3.5T$, the distribution function changes to a power law, as illustrated by the straight lines in log-log scale of Fig. 5.2. The upper part of the distribution does not collapse on a single line and changes from year to year. This shows that this part of the distribution is not stable in time.

Even though the fraction of population in the Pareto tail is small, their fraction f of the total income is significant, thus f can be thought of as a measure of income inequality. This fraction f is quite dynamic and sometimes changes significantly from year to year. One way to calculate f, is by constructing the so-called Lorenz curve [98]. It is defined parametrically in terms of the two coordinates $x(r)$ and $y(r)$ depending on the parameter r, which changes from 0 to ∞. The horizontal coordinate $x(r) = \int_0^r dr' P(r')$ is the fraction of population with income below r. The vertical coordinate $y(r) = \int_0^r dr' r' P(r') / \int_0^\infty dr' r' P(r')$ is the total income of this population, as a fraction of the total income in the system. An approximate formula for the Lorenz curve is [54]

$$y = (1 - f)[x + (1 - x)\ln(1 - x)] + f\Theta(x - 1), \tag{5.1}$$

where f is the fraction of the total income contained in the Pareto tail, and $\Theta(x-1)$ is the step function equal to 0 for $x < 1$ and 1 for $x \geq 1$. The Lorenz curve (5.1) experiences a vertical jump of the height f at $x = 1$, which reflects the fact that a small fraction of total population has a significant fraction of the total income. We made Lorenz curves for each year and found their best fits using Eq. 5.1. Fig. 5.3 shows typical Lorenz curves and their fits for two years. From the fits we obtained the values f. Fig. 5.4 shows the evolution of f over the last 24 years (f values for years 1983-2001 were obtained from Ref. [55]). Income inequality peaks during the speculative bubbles in the financial market. The peak in the year 2001 was due to the "dot-com bubble" and the peak in 2006 was due to the speculative bubble in the housing market.

In this section we extended the study of temporal evolution of income distribution in the USA [55] to the years 2002-2006. All our observations are in agreement with the results of Ref. [55], mentioned in the beginning. In addition we found that due to the speculative bubble in the housing market the income inequality peaked in the year 2006. We expect that the data for the subsequent years (when available) will show a decrease in income inequality, after the crash of that bubble in year 2007.

5.2 Modeling income distribution as a sum of additive and multiplicative stochastic processes

In section 5.1 we saw that income distribution follows a two-class structure. In this section we discuss a model which captures that feature. Consider a large number of agents among which there are pairwise transactions in which income is transferred from one agent to another. In the real world, money is regularly transferred from one agent to another in pairwise transactions, and it is not typical for agents to trade portions of their income. Nevertheless, indirect transfer of income may occur when one employee is promoted and another demoted while the total annual budget is fixed, or when one company gets a contract whereas another one loses it, etc. Let $P(r,t)$ be the the probability that at time t, an arbitrary agent may have income between r and $r+dr$. The time evolution of $P(r,t)$ is given by the master equation

$$\frac{\partial P(r,t)}{\partial t} = \int\limits_{-\infty}^{\infty} \left[-W(r,r')P(r,t) + W(r',r)P(r',t)\right] dr', \tag{5.2}$$

where $W(r,r')\,dr'\Delta t$ denotes the probability that in a short interval of time Δt an agent with income r makes a transition to an income between r' and $r'+dr'$. The first term in the integral in Eq. 5.2 corresponds to all those transitions that move agents with income r at time t to some other income r' and, hence, represent a loss to the function $P(r,t)$; similarly the second term in the integral corresponds to all those transitions that bring agents with income r' at time t to income r and, hence, represent a net gain to the function $P(r,t)$. We assume that only the transitions between nearby incomes have an appreciable probability of occurring; i.e, the transition probability $W(r,r')$ is sharply peaked around the value $r'=r$ and falls rapidly to zero away from r. Denoting the interval $\Delta r = r' - r$ by ξ we can write

$$W(r,r') \to W(r;\xi), \quad W(r',r) = W(r',-\xi),$$

where $W(r;\xi)$ and $W(r';-\xi)$ have sharp peaks around the value $\xi = 0$ and fall rapidly to zero elsewhere. Expanding right hand side of Eq. 5.2 in a Taylor series around $\xi = 0$ and retaining terms up to second order only we get

$$\frac{\partial P(r,t)}{\partial t} = \frac{\partial}{\partial r}\left[A(r)P(r,t)\right] + \frac{\partial^2}{\partial r^2}\left[B(r)P(r,t)\right], \tag{5.3}$$

where the coefficients $A(r)$ and $B(r)$ are the drift and the diffusion terms and are determined by the first and second moments of income changes per unit time

$$A(r) = \int_{-\infty}^{\infty} \xi W(r,\xi)\, d\xi = -\frac{\langle \Delta r \rangle}{\Delta t}, \tag{5.4}$$

$$B(r) = \int_{-\infty}^{\infty} \xi^2 W(r,\xi)\, d\xi = \frac{\langle (\Delta r)^2 \rangle}{2\Delta t}. \tag{5.5}$$

The stationary solution $\partial_t P = 0$ of Eq. (5.3) obeys

$$\frac{\partial (BP)}{\partial r} = -AP, \tag{5.6}$$

which has the general solution

$$P(r) = \frac{C}{B(r)} \exp\left(- \int^{r} \frac{A(r')}{B(r')} dr' \right). \tag{5.7}$$

Here C is a normalization function, such that $\int_0^\infty P(r)\, dr = 1$. Generally, the income of the people in the lower-class comes through wages, and salaries and it is reasonable to assume that their change in income is independent of income itself; i.e. Δr is independent of r, This process is called the additive diffusion [55]. In this case, the coefficients in Eq. (5.3) are constants A_0 and B_0. Then Eq. (5.7) gives the solution

$$P(r) = \frac{1}{T} \exp(-r/T_r), \quad T_r = B_0/A_0. \tag{5.8}$$

On the other hand, the income of the upper class comes from bonuses, investments, and capital gains [101], which are calculated in percentages. Therefore, for the upper class, it is reasonable to expect that $\Delta r \propto r$, i.e. income changes are proportional to income itself. This is known as the proportionality principle of Gibrat [?], and the process is called the multiplicative diffusion [55] (multiplicative hypothesis for the upper class was quantitatively verified in Refs. [99, 100] for Japan, where tax identification data is published for the top taxpayers). In this case, $A = ar$ and $B = br^2$, and Eq. (5.7) gives the power-law distribution $P(r) \propto 1/r^{\alpha+1}$ with $\alpha = 1 + a/b$.

However, the additive and multiplicative processes may coexist. An employee may receive a cost-of-living raise calculated in percentages (the multiplicative process) and a merit raise calculated in dollars (the additive process). In this case, we have $A = A_0 + ar$ and $B = B_0 + br^2 = b(r_0^2 + r^2)$, where $r_0^2 = B_0/b$. Substituting these expressions into Eq. (5.7), we find

$$P(r) = C \, \frac{e^{-(r_0/T_r)\tan^{-1}(r/r_0)}}{[1 + (r/r_0)^2]^{1+a/2b}}, \tag{5.9}$$

The distribution (5.9) interpolates between the exponential law for low r and the power law for high r, because either the additive or the multiplicative process dominates in the corresponding limit. The crossover between the two regimes takes place at $r \sim r_0$, where the additive and multiplicative contributions to B are equal. The distribution (5.9) has three parameters: the "income temperature" $T_r = A_0/B_0$, the Pareto exponent $\alpha = 1 + a/b$, and the crossover income r_0. It is a minimal model that captures the salient features of the empirical income distribution shown in Fig. 5.2.

We used Eq. (5.9) to fit the IRS data on personal income for the years 1996-2005. The cumulative distribution function $C(r) = \int_r^\infty P(r')\,dr'$ does not have an analytical form and has to be obtained by integrating $P(r)$ numerically, for a given set of parameters T_r, r_0, and α. Searching for the parameter values for which the numerically obtained $C(r)$ fits the empirical CDF best, becomes a computationally challenging task. We simplified this task in the following way. We chose the T_r values to be the same as the T values given in Fig. 5.2, and then obtained the other two parameters r_0 and α by minimizing the mean square error between the empirical and the theoretical CDF, in log-log scale. Fig. 5.5 shows the plots of the CDF and their best fits as function of r/T_r, in log-log scale. In these coordinates the data points and their fits collapse on each other in the low to middle income regime. For clarity's sake the data points and their fits are shifted vertically for successive years. Clearly, the theoretical curves agree very well with the empirical data. The values of the fitting parameters are listed in table 5.1.

To conclude, in this section we discussed a theoretical model which captures the two-class structure of income distribution in the USA. We obtained an analytical stationary solution of the Fokker-Planck equation for a stochastic process that is a sum of the additive and multiplicative processes. The stationary probability distribution function smoothly interpolates between an exponential distribution at the low end and a power law at the high end. It may have different applications in physics. Here we applied it to income distribution in a society by modeling income as a stochastic process. We analyzed the personal income distribution data in USA from the Internal Revenue Service. Using just three fitting parameters (the average income in the exponential part, the power-law exponent, and the crossover point between the exponential and the power laws), we obtained good fits of the IRS data for a range of years.

5.3 Distribution of annual income of UMD employees

In this section we analyze the annual salaries of University of Maryland employees, published in "The Diamondback" for the years 2007 & 2008. For these two years, the data sets contain the annual salaries of 6343 and 9119 employees respectively. Fig. 5.3 shows the plots of CDF for years 2007 & 2008 in log-linear scale. To show the data points clearly, the CDF for the year 2007 is shifted down by a factor of 10. In this scale most of the data points (except the ones at very low income) fall on a straight line for almost three orders of magnitude. This again suggests that the distribution of salaries is very well described by the exponential function. Also, notice that on the high income side there are only a few points which do not lie on the straight line. This implies that in this data set there is no power law tail, like the one present in the IRS data, see Fig. 5.2. These observations are in good agreement with the results of Ref. [55], that the lower-class people are the salary earners and they follow the exponential distribution (like the UMD employees), the upper-class people follow a power law and earn through investments and capital gains (not present among the UMD employees). Fig. 5.3 also shows the exponential fit to the relevant part of the CDF. The slope values obtained from the fits are slightly smaller than expected (compare them with the slopes for the IRS data), we do not have a good explanation for that.

At very low income the slope of $C(r)$ is smaller than what is predicted by the exponential distribution. In terms of $P(r)$ it means that at very low income, the value of the probability density is smaller than what is predicted by the exponential distribution. The PDF for the year 2008, shown in Fig 5.3, illustrates this fact. One simple reason for this discrepancy could be that in a data set like this, people with very low income get under sampled. On a larger data set, like the one from IRS, its clear that the probability density is maximum at very low income.

In conclusion, we found that the annual salary of UMD employees follows the exponential distribution and the employees are a good representation of the middle income range salary earners in the USA.

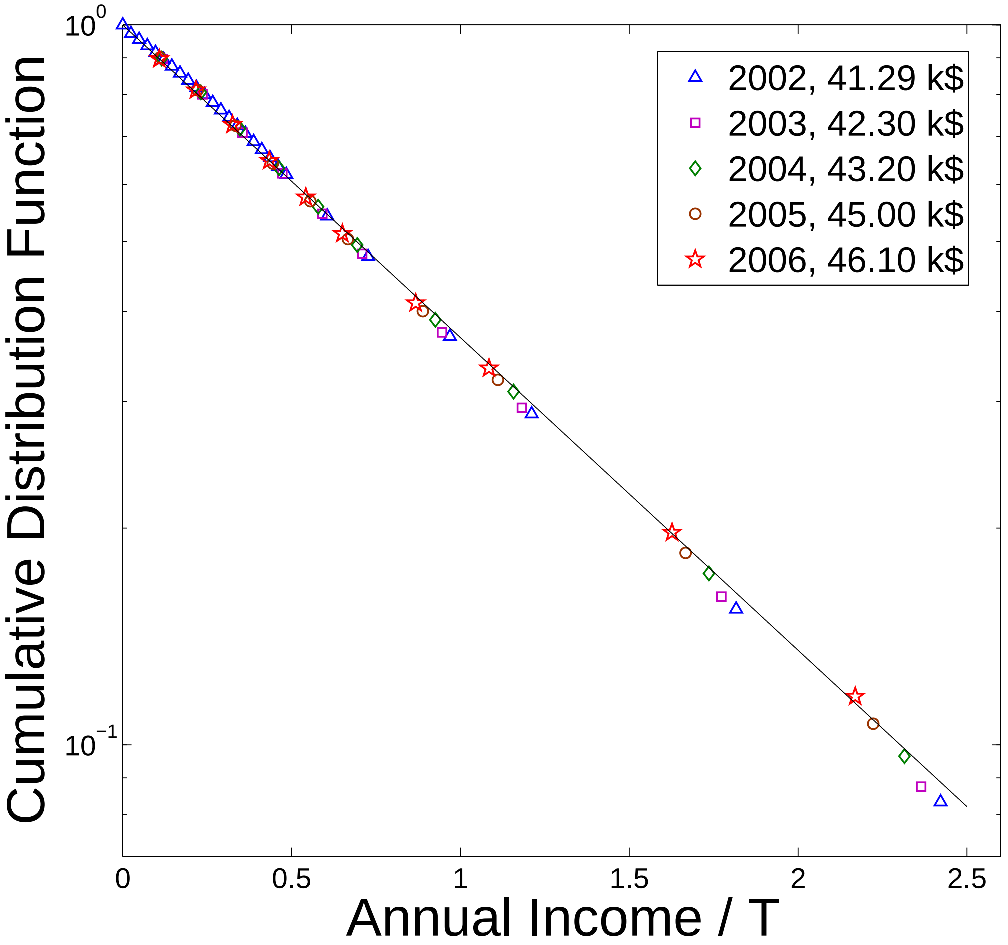

Figure 5.1: Figure shows the plot of cumulative probability $C(r)$ vs r/T in log-linear scale. The column of number gives the values of T for the corresponding year. The IRS data points are for the years 2002-2006.

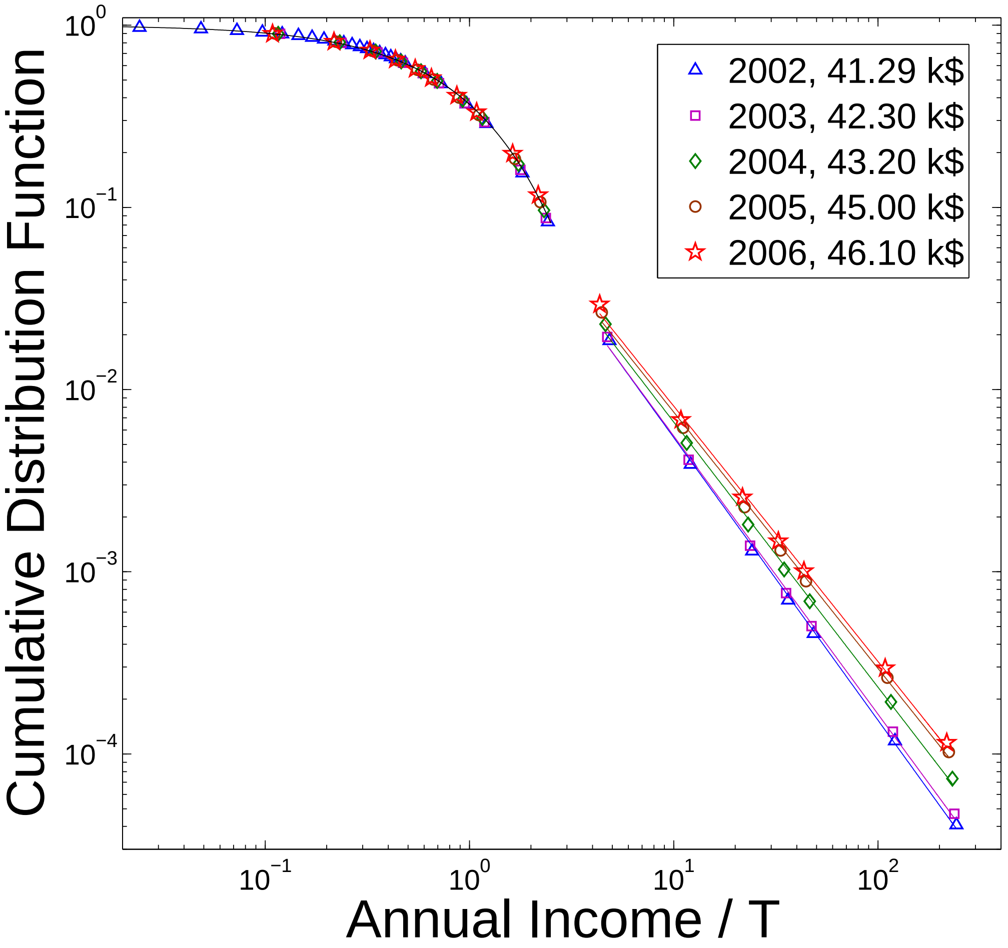

Figure 5.2: Figure shows the log-log plot of cumulative probability $C(r)$ vs r/T for a wider range of income.

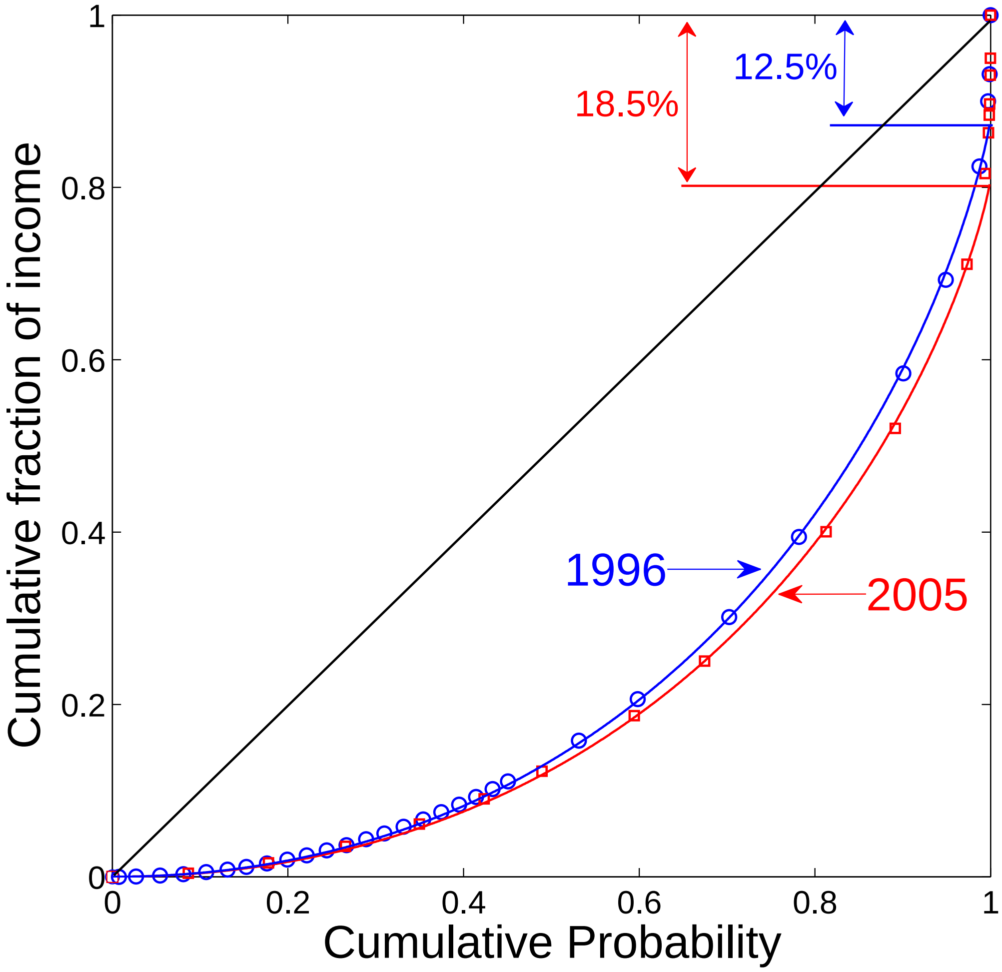

Figure 5.3: The figure shows the Lorenz curves for the years 1996 & 2005, and their fits obtained from Eq 5.1.

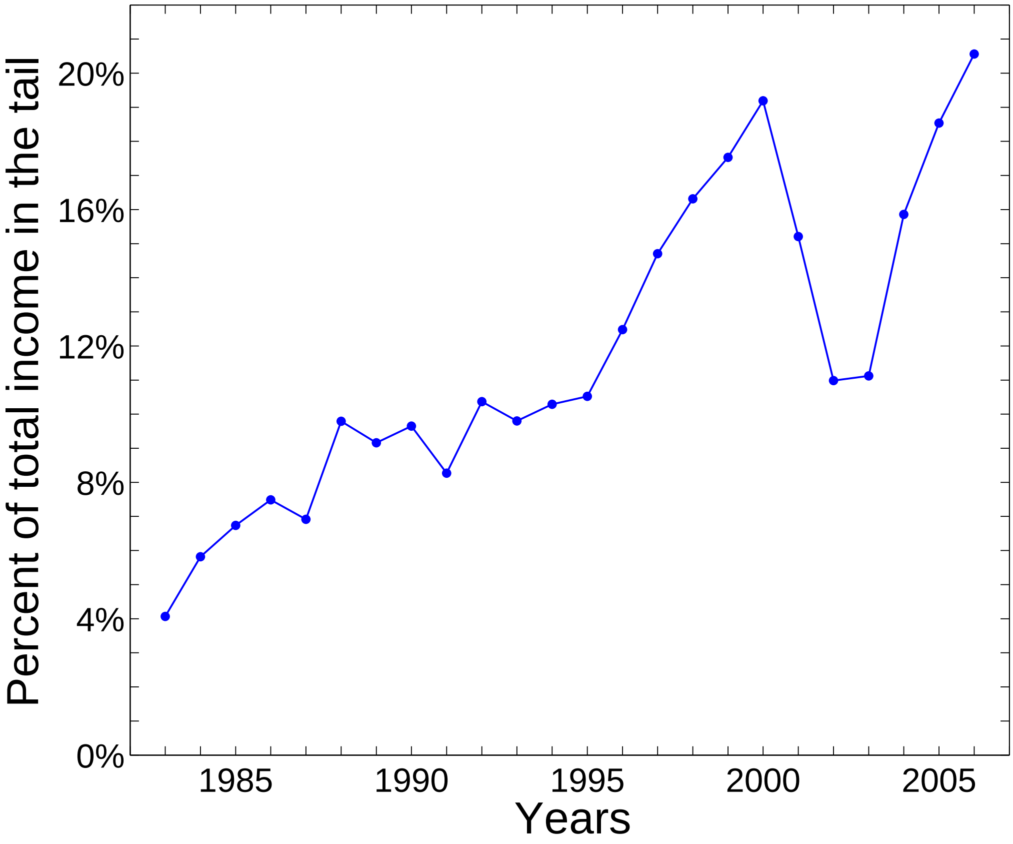

Figure 5.4: Figure shows the time evolution of f, the percentage of total in come in the power law tail.

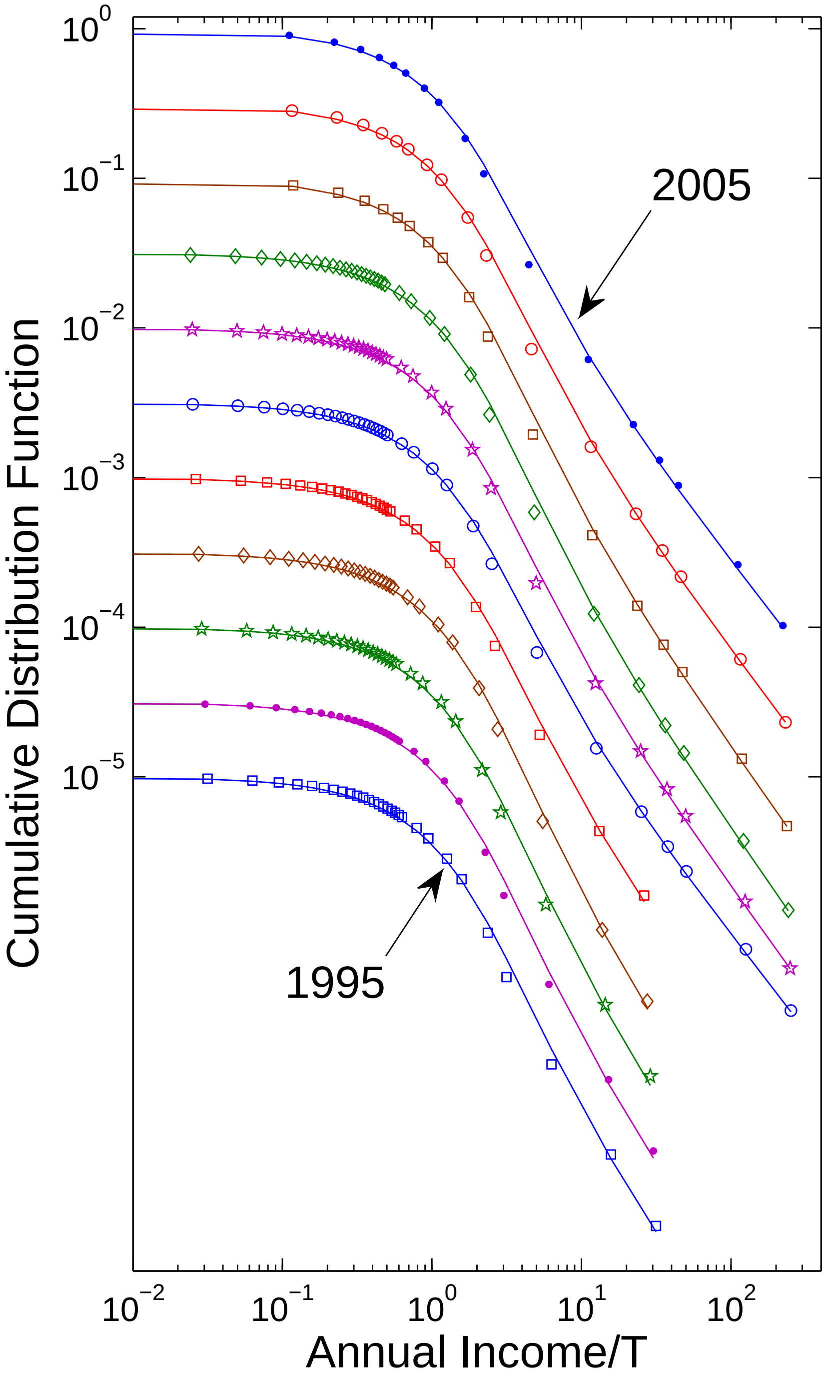

Figure 5.5: The figure show the cumulative probability $C(r)$ and their fits obtained from Eq. 5.9. To show the fits clearly, the data points and their fits are shifted vertically by a factor of $\sqrt{10}$ for successive years.

Table 5.1: Parameters values of the fits of IRS data, shown in Fig. 5.5. T_r values were obtained by fitting the lower part of the CDF with an exponential function. Values of r_0 and α we obtained by minimizing the mean square deviation between the empirical and theoretical CDFs, in log-log scale.

Year	T_r(k$)	r_0(k$)	α
1995	31.71	95	1.39
1996	32.99	100	1.41
1997	34.63	104	1.44
1998	36.33	111	1.45
1999	38.00	114	1.32
2000	39.76	119	1.26
2001	40.17	119	1.36
2002	41.29	126	1.41
2003	42.30	127	1.39
2004	43.20	131	1.31
2005	45.00	135	1.26

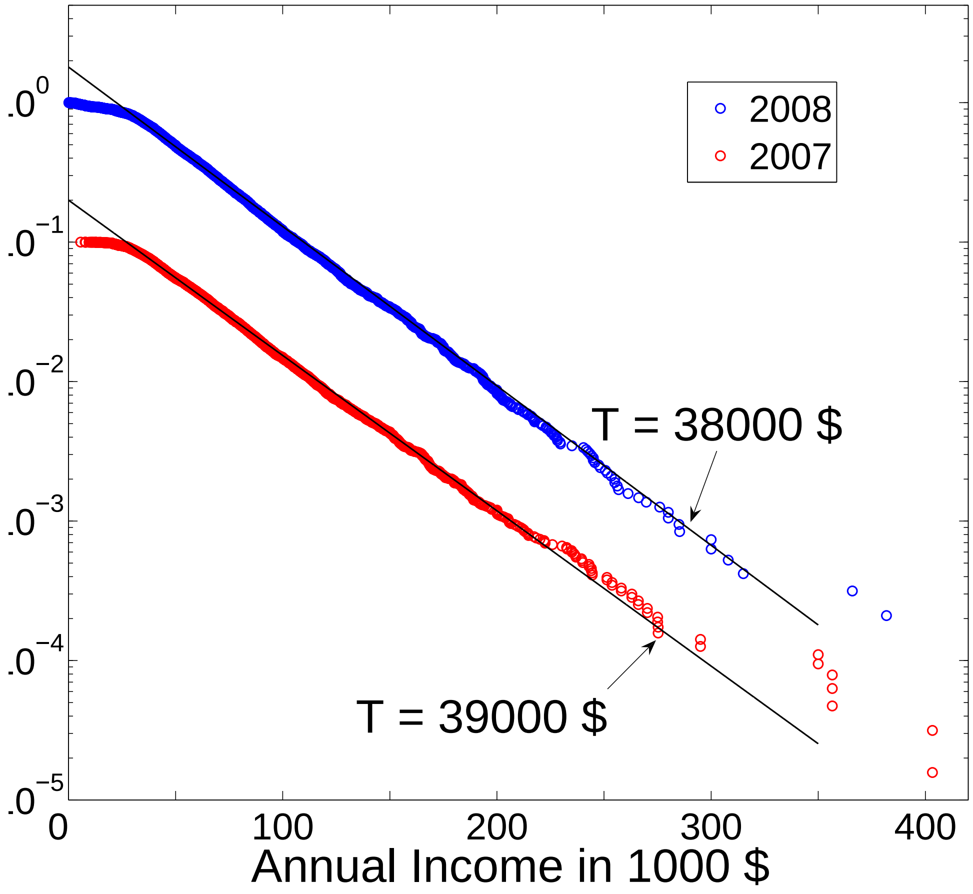

Figure 5.6: Plot of the cumulative distribution function of the annual salary of the university of Maryland employees.

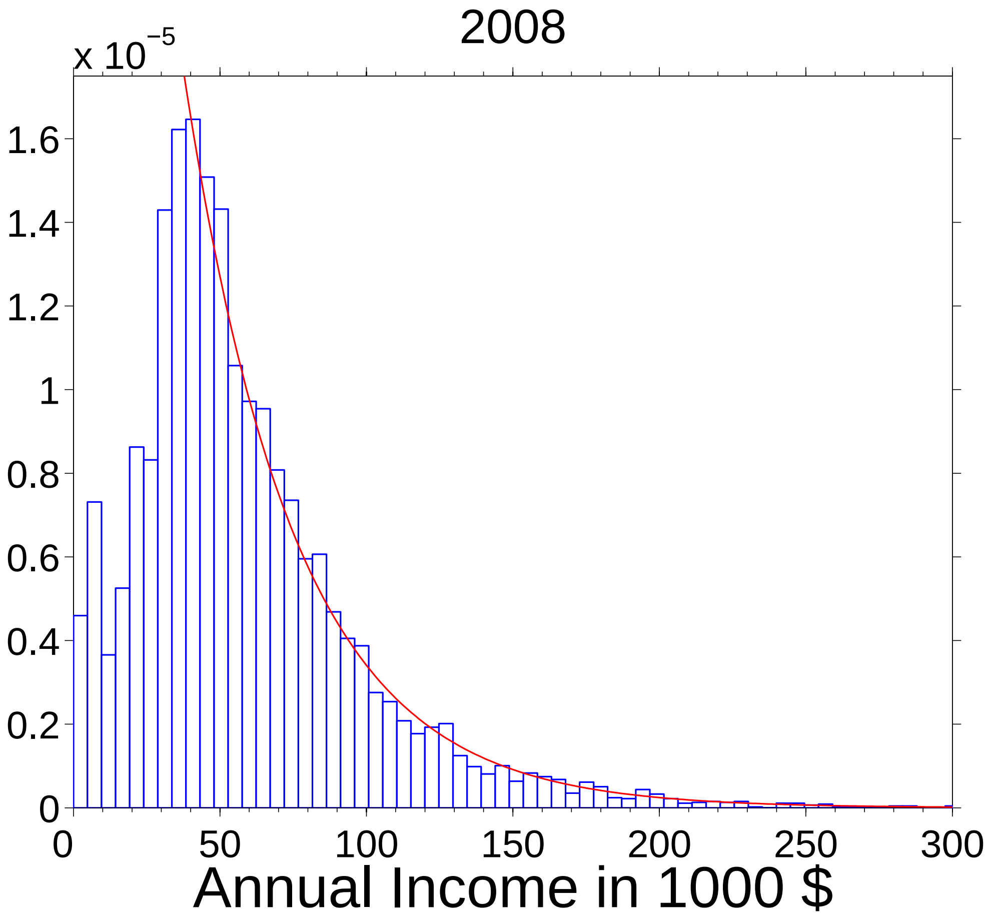

Figure 5.7: Figure shows the probability density of the annual salaries of the university of Maryland employees, for the year 2008.

BIBLIOGRAPHY

[1] T. Ishiguro, K. Yamaji, and G. Saito, *Organic Superconductors* (Springer, Berlin, 1998).

[2] *Physics of Organic Superconductors and Conductors*, edited by A.G. Lebed (Springer, Berlin, 2008).

[3] A.G. Lebed, JETP Letters **43**, 174 (1986); A.G. Lebed and P. Bak, Phys. Rev. Lett. **63**, 1315 (1989).

[4] T. Osada, A. Kawasumi, S. Kagoshima, N. Miura and G. Saito, Phys. Rev. Lett. **66**, 1525 (1991).

[5] M.J. Naughton, O.H. Chung, M. Chaparala, X. Bu and P. Coppens, Phys. Rev. Lett. **67**, 3712 (1991).

[6] E.I. Chashechkina and P.M. Chaikin, Phys. Rev. Lett. **80**, 2181 (1998)

[7] W. Kang, S.T. Hannahs, and P.M. Chaikin, Phys. Rev. Lett. **69**, 2827 (1992); D.G. Clarke *et al.*, Science **279**, 2071 (1998).

[8] K. Behnia, M. Ribault, and C. Lenoir, Europhys. Lett. **25**, 285 (1994).

[9] G.M. Danner, W. Kang, and P.M. Chaikin, Phys. Rev. Lett. **72**, 3714 (1994).

[10] G.M. Danner and P.M. Chaikin, Phys. Rev. Lett. **75**, 4690 (1995).

[11] H. Yoshino *et al.*, J. Phys. Soc. Jpn. **64**, 2307 (1995); **66**, 2248 (1997); **66**, 2410 (1997).

[12] T. Osada, S. Kagoshima, and N. Miura, Phys. Rev. Lett. **77**, 5261 (1996).

[13] A.G. Lebed and N.N. Bagmet, Phys. Rev. B **55**, R8654 (1997).

[14] I.J. Lee and M.J. Naughton, Phys. Rev. B **57**, 7423 (1998).

[15] I.J. Lee and M.J. Naughton, Phys. Rev. B **58**, R13343 (1998).

[16] W. Kang, T. Osada, Y.J. Jo, and H. Kang, Phys. Rev. Lett. **99**, 017002 (2007).

[17] W. Kang, Phys. Rev. B **76**, 193103 (2007).

[18] A. Ardavan *et al.*, Phys. Rev. Lett. **81**, 713 (1998); A.E. Kovalev, S. Hill, and J.S. Qualls, Phys. Rev. B **66**, 134513 (2002); Y. Oshima *et al.*, *ibid.* **68**, 054526 (2003); S. Takahashi *et al.*, J. Appl. Phys. **93**, 8665 (2003).

[19] S. Takahashi *et al.*, Phys. Rev. B **72**, 024540 (2005).

[20] S. Hill, Phys. Rev. B **55**, 4931 (1997).

[21] S.J. Blundell and J. Singleton, Phys. Rev. B **53**, 5609 (1996); S.J. Blundell, A. Ardavan, and J. Singleton, Phys. Rev. B **55**, R6129 (1997).

[22] S. Takahashi *et al.*, J. Low Temp. Phys. **142**, 315 (2006).

[23] S. Hill and S. Takahashi in [2], p. 457.

[24] W. Wu, P.M. Chaikin, W. Kang, J. Shinagawa, W. Yu, and S.E. Brown, Phys. Rev. Lett. **94**, 097004 (2005).

[25] T. Osada, S. Kagoshima, and N. Miura, Phys. Rev. B **46**, 1812 (1992).

[26] A.G. Lebed and M.J. Naughton, Phys. Rev. Lett. **91**, 187003 (2003).

[27] A.G. Lebed, H.I. Ha, and M.J. Naughton, Phys. Rev. B **71**, 132504 (2005).

[28] H.I. Ha, A.G. Lebed, M.J. Naughton, Phys. Rev. B **73**, 033107 (2006).

[29] T. Osada, N. Kamia, R. Kondoc and S. Kagoshima, Synth. Metals **103**, 2024 (1999).

[30] H. Yoshino and K. Murata, J. Phys. Soc. Jpn. **68**, 3027 (1999).

[31] H. Yoshino, A. Oda, T. Sasaki, T. Hanajiri, J. Yamada, S. Nakatsuji, H. Anzai and K. Murata, J. Phys. Soc. Jpn. **68**, 3142 (1999).

[32] K. Kobayashi, M. Saito, E. Ohmichi, and T. Osada, Phys. Rev. Lett. **96**, 126601 (2006).

[33] W. Shockley, Phys. Rev. **79**, 191 (1950).

[34] R.G. Chambers, Proc. Phys. Soc. A (London) **65**, 458 (1952).

[35] J.M. Ziman, *Principles of the Theory of Solids* (Cambridge University Press, Cambridge, 1972).

[36] R.H. McKenzie, P. Moses, Phys. Rev. Lett. **81**, 4492 (1998); Phys. Rev. B **60**, 7998 (1999); U. Lundin and R.H. McKenzie, *ibid.* **70**, 235122 (2004).

[37] T. Osada *et al.*, Synth. Metals **133–134**, 75 (2003); **135–136**, 653 (2003); Physica E **12**, 272 (2002); **18**, 200 (2003).

[38] B.K. Cooper and V.M. Yakovenko, Phys. Rev. Lett **96**, 037001 (2006).

[39] W.D. Oliver, Y. Yu, J.C. Lee, K.K. Berggren, L.S. Levitov, T.P. Orlando, *Science* **310**, 1653 (2005).

[40] D.M. Berns, W.D. Oliver, S.O. Valenzuela, A.V. Shytov, K.K. Berggren, L.S. Levitov, and T.P. Orlando, Phys. Rev. Lett **97**, 150502 (2006).

[41] M. Sillanpää, T. Lehtinen, A. Paila, Y. Makhlin, and P. Hakonen, Phys. Rev. Lett **96**, 187002 (2006).

[42] A. Izmalkov *et al.*, Phys. Rev. Lett. **101**, 017003 (2008).

[43] S. Ashhab, J.R. Johansson, A.M. Zagoskin, and F. Nori, Phys. Rev. A **75**, 063414 (2007).

[44] R.G. DeVoe, J. Hoffnagle, and R.G. Brewer, Phys. Rev. A **39**, 4362 (1989); R. Blümel, C. Kappler, W. Quint, and H. Walther, Phys. Rev. A **40**, 808 (1989).

[45] V. Pareto, Cours d'Économie Politique, Lausanne, 1897.

[46] R. Gibrat, Les Inégalités Économiques, Sirely, Paris, 1931.

[47] M. Kalecki, Econometrica **13**, 161 (1945).

[48] T. Di Matteo, T. Aste, S. T. Hyde, in The Physics of Complex Systems, edited by F. Mallamace and H. E. Stanley, IOS Press, Amsterdam, 2004, p. 435.

[49] W. Souma, Fractals 9 (2001) 293.

[50] F. Clementi, M. Gallegati, Physica A 350 (2005) 427.

[51] A. A. Drăgulescu, V. M. Yakovenko, Eur. Phys. J. B 17 (2000) 723.

[52] A. A. Drăgulescu, V. M. Yakovenko, Eur. Phys. J. B 20 (2001) 585.

[53] A. A. Drăgulescu, V. M. Yakovenko, Physica A 299 (2001) 213.

[54] A. A. Drăgulescu, V. M. Yakovenko, in Modeling of Complex Systems: Seventh Granada Lectures, edited by P. L. Garrido and J. Marro, AIP Conference Proceedings 661, New York, 2003, p. 180.

[55] A. C. Silva, V. M. Yakovenko, Europhys. Lett. 69 (2005) 304.

[56] J. Mimkes, Th. Fruend, G. Willis, cond-mat/0204234; G. Willis and J. Mimkes, cond-mat/0406694.

[57] N. Scafetta, S. Picozzi, B.J. West, Quantitative Finance **4**, 353 (2004).

[58] J. C. Ferrero, Physica A 341 (2004) 575.

[59] Econophysics of Wealth Distributions, edited by A. Chaterjee, S. Yarlagadda, B. K. Chakrabarti, Springer, Milan, 2005.

[60] W. Wu, I.J. Lee, and P.M. Chaikin, Phys. Rev. Lett. **91**, 056601 (2003); N.P. Ong, W. Wu, P.M. Chaikin, and P.W. Anderson, Europhys. Lett. **66**,579 (2004); W. Wu, N.P. Ong, and P.M. Chaikin, Phys. Rev. B **72**, 235116 (2005); E.S. Choi, J.S. Brooks, H. Kang, Y.J. Jo, and W. Kang, Phys. Rev. Lett. **95**, 187001 (2005); M.S. Nam, A. Ardavan, W. Wu, and P.M. Chaikin, Phys. Rev. B **74**, 073105 (2006); W. Wu and P.M. Chaikin, Phys. Rev. B **76**, 153102 (2007).

[61] W. Kang, Y.J. Jo, and H.Y. Kang, J. Phys. Conference Series **51**, 355 (2006).

[62] H. Kang, Y.J. Jo, S. Uji, and W. Kang, Phys. Rev. B **68**, 132508 (2003).

[63] E.I. Chashechkina and P.M. Chaikin, Phys. Rev. B **65**, 012405 (2001).

[64] K. Maki, Phys. Rev. B **45**, R5111 (1992).

[65] A.G. Lebed, N.N. Bagmet, and M.J. Naughton, Phys. Rev. Lett. **93**, 157006 (2004).

[66] A.G. Lebed, N.N. Bagmet, and M.J. Naughton, J. Phys. IV France **114**, 77 (2004).

[67] V.M. Yakovenko, Europhys. Lett. **3**, 1041 (1987); Sov. Phys. JETP **66**, 355 (1987).

[68] V.M. Yakovenko, Phys. Rev. Lett. **61**, 2276 (1988).

[69] A.G. Lebed, Phys. Rev. Lett. **95**, 247003 (2005).

[70] N. Joo *et al.*, Eur. Phys. J. B **52**, 337 (2006).

[71] Eq. (12) in Ref. [38] gives a similar expression for σ_{zz} in the case of multiple tunneling amplitudes t_l. However, it contains an error and should be replaced by the correct Eqs. (3.7) and (2.20) given here.

[72] In Secs. 2.3 and 2.5, we ignore the tunneling amplitude t_c' introduced in Sec. 2.2 and consider only the main amplitude t_c. The effects discussed in Secs. 2.3 and 2.5 can be obtained already at $t_c' = 0$.

[73] J.P. Eisenstein, T.J. Gramila, L.N. Pfeiffer, and K.W. West, Phys. Rev. B **44** 6511 (1991).

[74] J.A. Simmons, S.K. Lyo, J.F. Klem, M.E. Sherwin, and J.R. Wendt, Phys. Rev. B **47** 15741 (1993).

[75] V.M. Yakovenko and B.K. Cooper, Physica E **34**, 128 (2006).

[76] G.D. Mahan, *Many-Particle Physics*, 2nd ed. (Plenum Press, New York 1990).

[77] S. Haddad, S. Charfi-Kaddour, M. Hritier, and R. Bennaceur, Phys. Rev. B **72**, 085104 (2005).

[78] S. Uji, T. Terashima, H. Aoki, J.S. Brooks, S. Takasaki, J. Yamada, and H. Anzai, Phys. Rev. B **53**, 14399 (1996).

[79] W. Kang, S.T. Hannahs, and P.M. Chaikin, Phys. Rev. Lett. **70**, 3091 (1993); H. Shinagawa *et al.*, Physica B **201**, 490 (1994); Synth. Met. **70**, 759 (1995); E.I. Chashechkina and P.M. Chaikin, Phys. Rev. B **56**, 13658 (1997).

[80] H. Yoshino *et al.*, J. Phys. Conference Series **51**, 339 (2006); J. Low Temp. Phys. **142**, 323 (2007).

[81] P.A. Goddard, S.J. Blundell, J. Singleton, R.D. McDonald, A. Ardavan, A. Narduzzo, J.A. Schlueter, A.M. Kini, and T. Sasaki, Phys. Rev. B **69**, 174509 (2004).

[82] K.S. Novoselov, A.K. Geim, S.V. Morozov, D. Jiang, M.I. Katsnelson, I.V. Grigorieva, S.V. Dubonos and A.A. Firsov, *Nature* **438**, 197 (2005).

[83] Y. Zhang, Y.W. Tan, H.L. Stormer and P. Kim, *Nature* **438**, 201 (2005).

[84] K.S. Novoselov, E. McCann, S.V. Morozov, V.I. Fal'ko, M.I. Katsnelson, U. Zeitler, D. Jiang, F. Schedin and A.K. Geim, *Nature Physics* **2**, 177 (2006).

[85] M.V. Kartsovnik, P.A. Kononovich, V.N. Laukhin and I.F. Shchegolev, J. Exp. Theor. Phys. Lett. **48**, 541 (1998).

[86] K. Kajita, Y. Nishio, T. Takahashi, W. Sasaki, R. Kato, H. Kobayashi and Y. Iye, Solid State Commun. **70** , 1189 (1989).

[87] S.K. Lyo, Phys. Rev. B **57**, 9114 (1997).

[88] I. S. Gradshteyn, I. M. Ryzhik, *Tables of Integrals, Serise, and Products*, edited by A. Jeffrey (Academic Press, San Diego, 1994), 5th ed.

[89] P.R. Wallace, Phys. Rev. Lett. **71**, 622 (1947).

[90] T. Ando, T .Nakanishi and R. Saito, J. Phys. Soc. Jpn **67**, 2857 (1998).

[91] T. Ando, T .Nakanishi, J. Phys. Soc. Jpn **67**, 1704 (1998).

[92] C.L. Kane and E.J. Mele, Phys. Rev. Lett. **78**, 1932 (1997)

[93] E. McCann and V.I. Fal'ko, Phys. Rev. Lett. **96**, 086805 (2006).

[94] J. Nilsson, A.H. Castro Neto, N.M.R. Peres and F. Guinea, Phys. Rev. B **73**, 214418 (2006)

[95] J. B. McDonald, A. Mantrala, Journal of Applied Econometrics 10 (1995) 201.

[96] Champernowne DG (1953) A model of income distribution. The Economic Journal 63:318–351.

[97] http://www.diamondbackonline.com/

[98] N. Kakwani, *Income Inequality and Poverty* (Oxford University Press, Oxford, 1980).

[99] Fujiwara Y, Souma W, Aoyama H, Kaizoji T, Aoki M (2003) Growth and fluctuations of personal income. Physica A 321:598–604

[100] Aoyama H, Souma W, Fujiwara Y (2003) Growth and fluctuations of personal and company's income. Physica A 324:352–358

[101] Milaković M (2005) Do we all face the same constraints? In: Chatterjee A, Yarlagadda S, Chakrabarti BK (ed) Econophysics of Wealth Distributions, Springer, Milan, pp 184–191